Propulsion and Energy Forum
July 27-29, 2015, Orlando, FL
51st AIAA/SAE/ASEE Joint Propulsion Conference

A Discussion of Two Challenges of Non-Cooperative Satellite Refueling

Gregory T. Coll[1]
Orbital ATK, NASA Goddard Space Flight Center, Greenbelt, Maryland, 20771

Thomas J. Aranyos[2], Brian M. Nufer[3], and David Tomasic[3]
NASA Kennedy Space Center, Florida 32899

and

Max Kandula[4]
SGT Inc., NASA Kennedy Space Center, Florida 32899

Downloaded by NASA Kennedy Space Center on July 29, 2015 | http://arc.aiaa.org | DOI: 10.2514/6.2015-3952

There is recent interest from the government and commercial aerospace community in advancing propellant transfer technology for on-orbit refueling (servicing) of satellites. This paper introduces two challenges to a Propellant Transfer System (PTS) under development for demonstration of non-cooperative satellite servicing. The PTS is being developed to transfer storable propellant (heritage hypergolic fuels and oxidizers as well as xenon) safely and reliably from one servicer satellite to a non-cooperative existing client satellite. NASA is in the project evaluation and planning stages for conducting an on-orbit demonstration to an existing government asset to prove these technologies. The PTS will manage pressure, flow rate, temperature, mass totalization, and other parameters to control the condition of the propellant being transferred to the client. A major challenge is to design a safe, reliable system with some new technologies while maintaining a reasonable cost. Two particular technology challenges are venting of liquid jets in space and mass flow measurement accuracy.

Nomenclature

c	=	specific heat at constant pressure (kJ/kg.K)
h_{fg}	=	latent heat of vaporization (kJ/kg)
Ja	=	Jacob number (dimensionless), $\rho_f c_f \Delta T_{\sup} / (\rho_v h_{fg})$
k	=	thermal conductivity (W/m.K)
L_b	=	jet burst length (m)
M	=	molecular weight (kg/mol)
$\dot{m}_g$	=	mass transfer (evaporation) rate, (kg/m^2.s)
p	=	pressure (Pa)
p_v	=	vapor pressure (Pa)
$\dot{Q}$	=	heat conducted into the bubble per unit time
q	=	heat flux (W/m^2)
$R(t)$	=	instantaneous bubble radius (m)
$\dot{R}, \ddot{R}$	=	first and second derivatives of bubble radius with respect to time, respectively

[1] Propulsion Manager, Satellite Servicing Capabilities Office, Mail Stop 408, Senior Member, AIAA
[2] Technical Integration Manager, Systems Engineering, Mail Stop NE-T3.
[3] Project Engineer, Fluids Division, Mail-Stop NE-M4.
[4] Subject Matter Expert, Fluids and Propulsion Group, Mail-Stop ESC-630, Associate Fellow, AIAA.

Copyright © 2015 by the American Institute of Aeronautics and Astronautics, Inc. The U.S. Government has a royalty-free license to exercise all rights under the copyright claimed herein for Governmental purposes.

R_c	=	critical bubble radius (m)
$\overline{R}$	=	universal gas constant (kJ/kmol.K)
r	=	radial coordinate from the center of the bubble
T	=	temperature (K)
t	=	time (s)
t_b	=	jet burst time (s)
t_d	=	delay period for bubble growth (s)
V_0	=	jet initial velocity (m/s)
x	=	coordinate distance along the jet centerline from the nozzle exit (m)
BFM	=	balanced orifice flow meter
CFC-113	=	trichlorotrifluoroethane (Freon-113)
DP	=	Delta pressure
FM	=	flow meter
gpm	=	gallons per minute
KSC	=	Kennedy Space Center
LPM	=	liters per minute
MMH	=	monomethylhydrazine
N_2H_4	=	hydrazine
N_2O_4	=	nitrogen tetroxide
NTO	=	nitrogen tetroxide (N_2O_4)
psid	=	pounds per square inch delta
PTA	=	propellant transfer assembly
PTS	=	propellant transfer system
RPM	=	Revolutions per minute
UFM	=	ultrasonic flow meter
LEO	=	low earth orbit
GEO	=	geosynchronous earth orbit
MSFC	=	Marshall Space Flight Center
JSC	=	Johnson Space Center

Greek Symbols

Δp_∞	=	initial pressure difference, $p_v(T_\infty) - p_\infty$
$\Delta T_{\sup}$	=	bulk liquid superheat, $T_\infty - T_{sat}(p_\infty)$
α	=	thermal diffusivity (m^2/s)
ν	=	kinematic viscosity (m^2/s)
ρ	=	density (kg/m^3)
σ	=	surface tension (N/m)
θ	=	burst cone (included) angle (deg)

Subscripts

0	=	inlet, initial
∞	=	far from the bubble (value at large r)
b	=	jet burst condition
c	=	critical (bubble size)
eq	=	equilibrium
f	=	liquid
g	=	vapor
s	=	jet surface
sat	=	value at saturation
sup	=	superheat
tp	=	triple point
v	=	vapor

Downloaded by NASA Kennedy Space Center on July 29, 2015 | http://arc.aiaa.org | DOI: 10.2514/6.2015-3952

Downloaded by NASA Kennedy Space Center on July 29, 2015 | http://arc.aiaa.org | DOI: 10.2514/6.2015-3952

I. Introduction

Propellant Transfer System (PTS) technology for on-orbit servicing of satellites and spacecraft is of great contemporary interest. It is readily applicable to various storable propellants such as hypergolic oxidizer, monomethylhydrazine/MMH, hydrazine, and xenon. Suitable orbits for PTS technology include low earth orbit (LEO), geosynchronous orbit (GEO), or deep space fueling locations. Of the various technology challenges of on-orbit servicing, the team has made significant advancements in modeling trapped volume venting and flow metering / totalization accuracy.

As currently envisioned, there will be planned operational release(s) of clean and hypergolic contaminated GHe pressurant as well as small (several cubic centimeters) trapped volumes of liquid propellant during servicing operations. This paper covers specific analytical modeling techniques (based on common available flow programs) being utilized by NASA to model vent dispersions to ensure proper design for protection of client satellite and satellite servicer assets.

In addition, a spacecraft designed to service propellant onto multiple clients throughout its service life will require a highly accurate flow metering / totalization method. This will be used to maximize the knowledge of the transferred propellant to the client and minimize the amount of propellant originally required to be stored in the servicing / supply vehicle for cost effectiveness to multiple clients. This paper discusses specific flow metering technologies being evaluated and tested with simulant fluids and actual hypergolic propellant commodities. Significant findings from the test program will be presented.

II. The Challenge of On-Orbit Fluid Venting

THE phenomenon of flashing of high pressure liquid jets discharged into low pressure environment is of great practical interest in many areas of technology. Flashing jets present themselves in applications including chemical spills, desalination, and discharge of surplus water, propellants or other fluids in spacecraft operations. There exists the risk of surface contamination (to servicer or client) and fluid freezing near the nozzle exit when fluids are discharged into vacuous space. A fundamental understanding of the physics of flashing jets is requisite in the optimum design of nozzle configurations and jet parameters.

When a fluid is discharged into a low pressure environment or vacuum conditions through an axisymmetric orifice or nozzle, several interesting physical processes are manifested (Fig. 1), as first described by Fuchs and Legge[1]. The relevant pressure-volume diagram is shown in Fig. 2a (Blander and Katz[2]), and the pressure-temperature diagram is sketched in Fig. 2b.

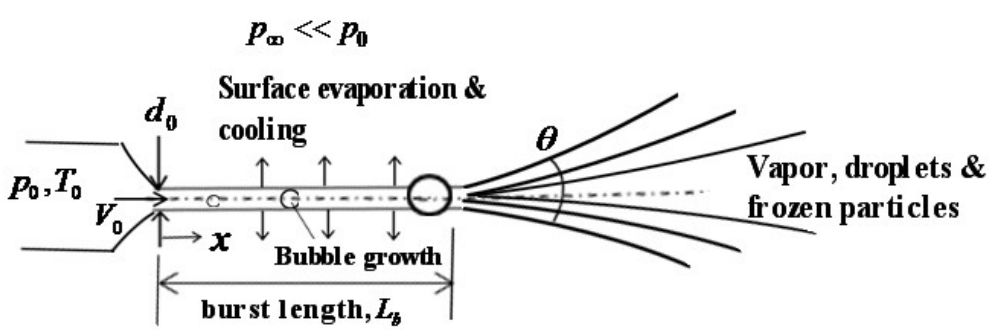

Figure 1. Schematic representation of a flashing liquid jet (after Fuchs and Legge[1]).

Downloaded by NASA Kennedy Space Center on July 29, 2015 | http://arc.aiaa.org | DOI: 10.2514/6.2015-3952

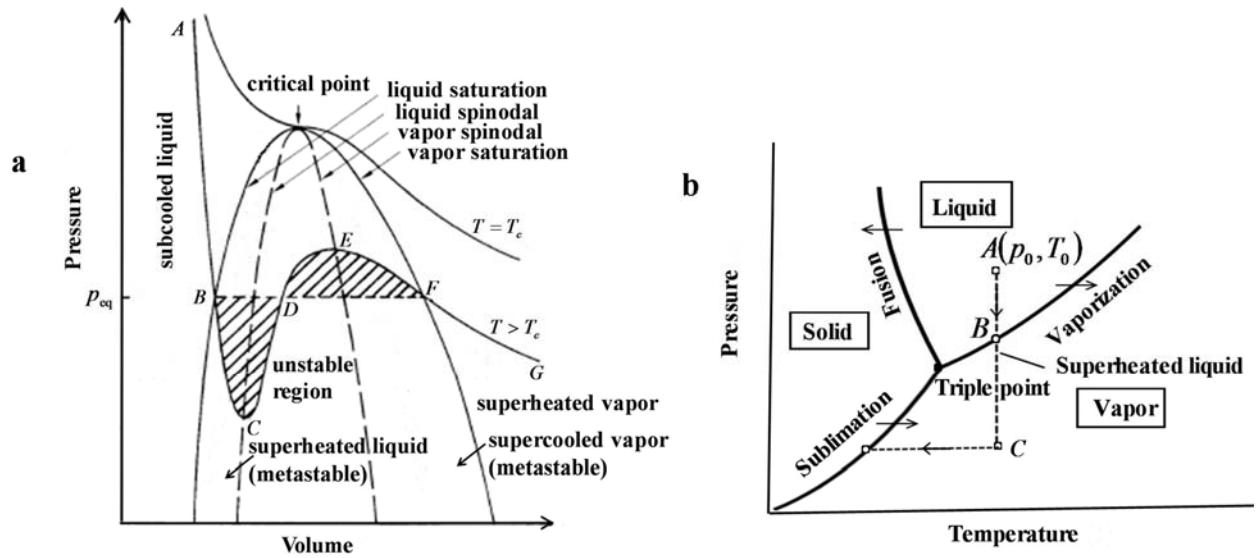

Figure 2. a) Pressure-volume diagram (after Blander and Katz[2]), b) Pressure-temperature diagram.

Immediately upon exit (Fig. 2), the subcooled liquid jet, initially at state A, crosses the saturation curve (State B) and becomes superheated (BC). Concurrently, surface evaporation takes place, which tends to cool the jet surface due to the energy lost by evaporation, with possible freezing of the remaining liquid. At sufficiently high superheats, bubble nucleation is initiated within the jet, and bubble growth takes place (following a delay period due to surface tension) on account of liquid inertia and heat conduction as it is convected downstream. The jet is initially straight, and its diameter diminishes due to surface evaporation. When the bubble grows beyond certain size sufficiently exceeding the local jet diameter, jet bursting occurs accompanied by droplet splash, and a cone of dispersion is observed which contains cloud of vapor, droplets and frozen particles. Under certain circumstances droplets deposit near the nozzle, subsequently freeze, and tend to plug the flow, which can be catastrophic in the case of spacecraft operations. There is also the possibility that the droplets and ice particles contaminate the neighboring surfaces of the spacecraft, altering its surface radiative properties[1].

An accurate prediction of the jet bursting lengths, included cone angle of jet expansion (disintegration or dispersion), and the resulting distribution of droplets and frozen particles is essential for a safe and efficient design of the venting systems. In view of the complex physical processes involved, the characterization of the flashing liquid jets on a theoretical front is exceedingly difficult, and very few studies have been reported in the literature. Most of the published studies are primarily experimental. Excellent reviews on the topic are presented by Fuchs and Legge[1] and Sher et al.[3], among others.

Fuchs and Legge[1], in their benchmark review and investigation on the topic, provided experimental data for water jets discharged into vacuum. The jet bursting distances and included angles could be derived based on the photographic studies. Different initial jet temperatures were considered. They called attention to the fact that the jet stream cools due to surface evaporation. The surface temperature history was approximately modeled from the solution of heat conduction equation in a semi-infinite slab, with the surface losing heat by evaporation. However the bubble dynamics and jet flashing was not theoretically addressed.

Muntz and Orme[4], in their detailed theoretical study, considered stream bursting on account of cavitation (bubble growth) and surface cooling effects. They considered Rayleigh-Plesset equation governing bubble dynamics, including surface tension and viscous effects (but neglecting heat diffusion effects), and estimated jet bursting distances on the predication that jet bursting is occasioned when the bubble grows to a size equal to the jet diameter. The predicted burst distances are an order of magnitude smaller than the data of Fuchs and Legge[1].

The purpose of this work is to formulate an improved analytical model for flashing liquid jets, accounting for bubble growth including the effects of surface tension, inertia, and heat-diffusion effects. The proposed bubble growth model for unbounded fluids, when appropriately modified and extended for circular jets (see Section B.2 for details), is able to explain satisfactorily the characteristics of flashing liquid jets, with emphasis on jet bursting distance and the cone angle of dispersion.

Downloaded by NASA Kennedy Space Center on July 29, 2015 | http://arc.aiaa.org | DOI: 10.2514/6.2015-3952

A. Brief Review of Bubble Growth Models

After the vapor nucleus has attained a size exceeding that for unstable equilibrium (critical bubble radius) the bubble will grow spontaneously following a temperature (or pressure) disturbance from equilibrium. The growth may be limited by surface tension, inertia of the surrounding liquid or the rate at which the latent heat of vapor is conducted to the vapor-liquid interface (Collier[5]). It is known that the early stages of bubble growth are controlled by surface tension and liquid inertia, and as the bubbles grow larger the pressures inside and outside the bubble tend to equalize and bubble growth by vaporization is controlled by the rate at which heat is conducted at the bubble boundary[5]. In the intermediate size range, the bubble growth is controlled by both inertia and heat diffusion (Lee and Merte[6]). As either the liquid superheat increases or the system pressure decreases, the bubble growth tends to become inertia controlled, and as either the liquid superheat decreases or the system pressure increases, the bubble growth tends to become heat diffusion controlled (Lee and Merte[6]).

In view of the fundamental importance of bubble growth modeling for the characterization of flashing liquid jets, we present a brief summary of the models for bubble growth in an unbounded medium with uniform superheat. A general representation of bubble dynamics is indicated in Fig. 3.

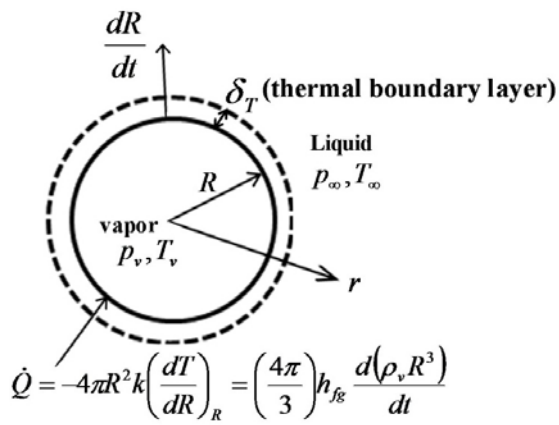

Figure 3. Model for bubble growth in a uniformly superheated liquid.

1 The Rayleigh Equation for Inertia Controlled Bubble Growth

Starting from the continuity and the momentum equations (Navier-Stokes equations), Lord Rayleigh[7] derived the following equation of motion for spherical bubble growth (or collapse) in an unbounded incompressible medium that is at rest at infinity at a pressure p_∞, neglecting the effects of surface tension, viscosity, and heat-diffusion , see Collier[5]:

$$R\ddot{R} + (3/2)\dot{R}^2 = \Delta p / \rho_f \tag{1a}$$

where $R(t)$ is the instantaneous bubble radius, $\dot{R} = dR/dt$, t is the time, ρ_f is the density of the liquid. The quantity Δp denotes the difference between the liquid pressure at the bubble boundary $p(R,t)$ and the liquid pressure at great distance from the bubble p_∞:

$$\Delta p = p(R) - p_\infty \tag{1b}$$

The pressure at the bubble boundary $p(R)$ is taken as the *vapor pressure* in the bubble p_v:

$$p(R) = p_v \tag{1c}$$

The initial conditions taken are

$$R = 0, \ \dot{R} = 0 \quad @\, t = 0 \tag{1d}$$

Assuming Δp as *constant*, and neglecting the term $R\ddot{R}$, Eq. (1a) is integrated for the radial bubble velocity dR/dt:

$$\frac{dR}{dt} = \left[\frac{2}{3}\frac{p_v - p_\infty}{\rho_f}\right]^{1/2} \tag{2}$$

Eq. (2) can be integrated to yield the instantaneous bubble radius

$$R = \left[\frac{2}{3}\frac{p_v - p_\infty}{\rho_f}\right]^{1/2} t \tag{3}$$

Eq. (3) represents *inertia controlled bubble growth* (so-called *isothermal bubble growth*), and is known to be valid in the early stages of bubble growth (small times), controlled by inertia.

2 *The Rayleigh-Plesset Equation*

From elementary physics a fluid exerts a pressure $2\sigma / R$ on account of surface tension inside a spherical cavity of radius R, where σ stands for the liquid-vapor surface tension. The pressure in the liquid adjacent to the bubble wall $p(R,t)$ is now expressed by

$$p(R,t) = p_v(R,t) - 2\sigma / R \tag{4a}$$

instead of Eq. (1c). Thus an extended form of Rayleigh equation, Eq. (1a), due to Plesset[8] takes the form

$$\rho_f\left[R\ddot{R} + \frac{3}{2}\dot{R}^2\right] = \left[p_v(R,t) - \frac{2\sigma}{R}\right] - p_\infty = \Delta p - \frac{2\sigma}{R} \tag{4b}$$

where

$$\Delta p = p_v - p_\infty \tag{4c}$$

Eq. (4b) represents the equilibrium of forces exerted by the bubble on the fluid pressure (pressure force), and the forces exerted by the fluid by surface tension and by inertia (term containing the density).

The initial condition $R = 0$ at $t = 0$ in Eq. (1d) is not physically realistic in view of the critical (minimum) bubble radius R_c (required for bubble growth) from thermodynamic stability arguments, which is defined by mechanical equilibrium consideration (set the inertia term to zero in Eq. 4b):

$$R_c = \frac{2\sigma}{p_v - p_\infty} \tag{4d}$$

The stability condition demands that bubbles with radius less than R_c tend to collapse, and those with a radius greater than R_c tend to grow. The appropriate initial condition now becomes

$$R = R_c, \;\; \dot{R} = 0 \quad @\, t = 0 \tag{4e}$$

Since heat is necessarily transferred to the bubble (for vapor generation) while it grows, the pressure at the bubble boundary (and thus the pressure drop Δp) will obviously vary with time according to the laws of thermodynamics (Forster and Zuber[9]). The pressure difference Δp is related to the temperature difference ΔT (difference in saturation temperature inside the bubble and that at great distance from the bubble), defined by

$$\Delta T = T_{\text{sat}}(p_v) - T_{\text{sat}}(p_\infty) = T_v - T_{\text{sat}}(p_\infty) \tag{5a}$$

The $\Delta p - \Delta T$ relation (along the saturation line) is governed by the thermodynamics of the process, namely the Clausius-Clapeyron equation,

Downloaded by NASA Kennedy Space Center on July 29, 2015 | http://arc.aiaa.org | DOI: 10.2514/6.2015-3952

$$\frac{dp}{dT} = \frac{h_{fg}}{T\left(v_f - v_g\right)} \tag{5b}$$

where h_{fg} is the latent heat of vaporization, v_f, v_g are the specific volumes of the liquid and the vapor respectively. In integrated form with constant properties at p_∞ and T_{sat}, the Clausius-Clapeyron equation becomes (Forster and Zuber[9]):

$$\Delta p = \Delta T \frac{h_{fg}}{T\left(v_f - v_g\right)} \quad \text{or} \quad p_v - p_\infty \approx \frac{\rho_v h_{fg}}{T_{\text{sat}}}\left(T_v - T_{\text{sat}}\right) \tag{5c}$$

The integrated Clausius-Clapeyron equation is only an approximation of the exact vapor pressure curve in view of the constant property assumption.

The temperature difference ΔT (or the temperature T_v) is obtained by the solution of the energy equation for the temperature distribution in the liquid region with a moving boundary (surface of evaporation) in conjunction with the momentum equation. In general, the vapor pressure and temperature at the bubble boundary could assume values in the following range: $p_\infty \le p_v \le p_{\text{sat}}\left(T_\infty\right)$, $T_{\text{sat}} \le T_v \le T_\infty$, where T_∞ represents the temperature of the liquid far from the bubble. As a result of evaporation, the liquid near the bubble boundary is cooled, and when the cooling effects become important, the bubble growth velocity $\dot{R}$, which is relatively high in the initial stage, as given by Eq. (2), is considerably reduced.

3 *Plesset-Zwick Solution for Heat-Diffusion Controlled Region*

The energy equation (in the liquid region) in spherical coordinates is expressed by

$$\frac{\partial T}{\partial t} + u_r \frac{\partial T}{\partial r} = \alpha_f \left(\frac{\partial^2 T}{\partial r^2} + \frac{2}{r}\frac{\partial T}{\partial r} \right) \tag{6a}$$

where α_f refers to the thermal diffusivity of the liquid, and

$$u_r = \varepsilon \frac{R^2}{r^2}\frac{dR}{dr}, \quad \varepsilon = \left(1 - \frac{\rho_v}{\rho_r}\right) \tag{6b}$$

The initial condition is

$$T\left(r,0\right) = T_\infty \tag{6c}$$

The thermal boundary conditions are

$$T\left(\infty,t\right) = T_\infty, \quad 4\pi R^2 k_f \left(\frac{\partial T}{\partial r}\right)_{r=R} = h_{fg}\frac{d}{dt}\left(\frac{4}{3}\pi R^3 \rho_v\right) \tag{6d}$$

The second boundary condition in Eq. (6d) states that the heat conducted from the liquid into the vapor bubble (in accordance with Fourier's law) is expended to vaporize the liquid.

Plesset and Zwick[10] derived a zero-order solution for the bubble wall temperature from the energy equation, assuming a thin thermal boundary layer (whose thickness is small relative to the bubble radius), and taking $\varepsilon = 1$ in Eq. (6b):

$$T\left(R\right) = T_\infty - \left(\frac{\alpha_f}{\pi}\right)^{1/2} \int_0^t \frac{R^2\left(x\right)\left(\partial T/\partial r\right)_{r=R(x)}}{\left(\int_x^t R^4\left(y\right)dy\right)^{1/2}} dx \tag{7}$$

The thin thermal boundary layer assumption is justified physically on the grounds that the thermal diffusivity of the liquid is small. Eq. (7) for $T\left(R\right)$ thus provides $p_v\left(T\right)$ in Eq. (4b), so that Eqs. (4b) and (7) constitute a set of coupled equations governing the dynamics of bubble growth, which can be solved only numerically.

Downloaded by NASA Kennedy Space Center on July 29, 2015 | http://arc.aiaa.org | DOI: 10.2514/6.2015-3952

Plesset and Zwick[11] later derived an *asymptotic solution* for bubble growth ($R >> R_c$) for this zero-order solution, valid for sufficiently large times (heat-diffusion controlled bubble growth regime neglecting liquid inertia, assuming a linear variation of vapor pressure with temperature; (Collier[5], Lee and Merte[6]):

$$\frac{dR}{dt} = \frac{1}{2}\left(\frac{12\alpha_f}{\pi t}\right)^{1/2} Ja \tag{8a}$$

where the Jacob number Ja (representing the ratio of sensible heat to the latent heat transfer) is defined by

$$Ja = \frac{\rho_f c_f \Delta T_{\text{sup}}}{\rho_v h_{fg}}, \quad \Delta T_{\text{sup}} = T_\infty - T_{\text{sat}}(p_\infty) \tag{8b}$$

The growth velocity, given by Eq. (8a) is seen to be much smaller than that corresponding to inertia growth, Eq. (2). The Plesset and Zwick[11] asymptotic solution for the bubble radius thus becomes (with $R = 0 @ t = 0$)

$$R = 2\left(\frac{3}{\pi}\alpha_f t\right)^{1/2} Ja \tag{9}$$

Forster and Zuber[9] and Birkhoff et al.[12] obtained approximate solutions, which are in close agreement with the Plesset-Zwick solution[11]. For example, Forster and Zuber[9] obtained the solution as

$$R = 2\left(\frac{\pi}{2}\alpha_f t\right)^{1/2} Ja \tag{10}$$

Scriven[13] solved the energy equation without the assumption of a thin boundary layer, and the asymptotic solution for moderate superheats was *identical* to that of Plesset and Zwick[11].

4 Mikic, Rohsenow and Griffith Model

Mikic et al.[14] have proposed a single closed-form (analytical) expression for bubble growth in combined inertia and heat-diffusion controlled regimes by effectively combining the two growth rate equations corresponding to the inertia regime (Rayleigh solution, Eq. (2)) valid for small times and heat-diffusion controlled regime (Plesset and Zwick solution, Eq. 8a)) valid for large times. For brevity this model will be referred to as the MRG model. It considers integrated form of the Clausius-Clapeyron equation with constant properties evaluated at the saturation temperature, see Eq. (5c). Replacing T_{sat} in Eq. (8b) by T_v, and then eliminating T_v with the help of Eq. (5c), the result becomes

$$R^+ = \frac{2}{3}\left[\left(t^+ + 1\right)^{3/2} - \left(t^+\right)^{3/2} - 1\right] \tag{11a}$$

where the dimensionless bubble radius R^+ and the dimensionless time t^+ are defined by

$$R^+ = \frac{A}{B^2}R, \; t^+ = \left(\frac{A}{B}\right)^2 t \tag{11b}$$

and

$$A = \left(\frac{2}{3}\frac{h_{fg}\rho_v \Delta T_{\text{sup}}}{\rho_f T_{\text{sat}}}\right), \; B = \left(\frac{12}{\pi}\alpha_f\right)^{1/2} \frac{c_f \rho_f \Delta T_{\text{sup}}}{h_{fg}\rho_v} \tag{11c}$$

For $t^+ << 1$ (small times), Eq. (11a) simplifies to the Rayleigh solution[7] for the inertia-controlled regime, Eq. (3):

$$R^+ = t^+ \quad \text{or} \quad R = At \tag{12a}$$

Downloaded by NASA Kennedy Space Center on July 29, 2015 | http://arc.aiaa.org | DOI: 10.2514/6.2015-3952

For $t^+ >> 1$ (large times), it reduces to the asymptotic solution of Plesset and Zwick [11] for the heat diffusion-controlled regime, Eq. (9):

$$R^+ = \sqrt{t^+} \quad \text{or} \quad R = B\sqrt{t} \tag{12b}$$

In an effort to examine the applicability of various analytical formulations for bubble growth, including the MRG model, Lee and Merte[6] presented numerical solutions (of momentum and energy equations) for vapor bubble growth in an initially uniformly superheated liquid including the effects of surface tension, liquid inertia, and heat diffusion, with the Landau transformation considered to immobilize the moving boundary. It was shown that the bubble radius and velocity curves converge quite well to the solution from the MRG model except for the early stage of growth, where the delay period due to surface tension effects (extremely slow growth) become important (Fig. 4). It was shown that the delay period increases with a decrease in liquid superheat.

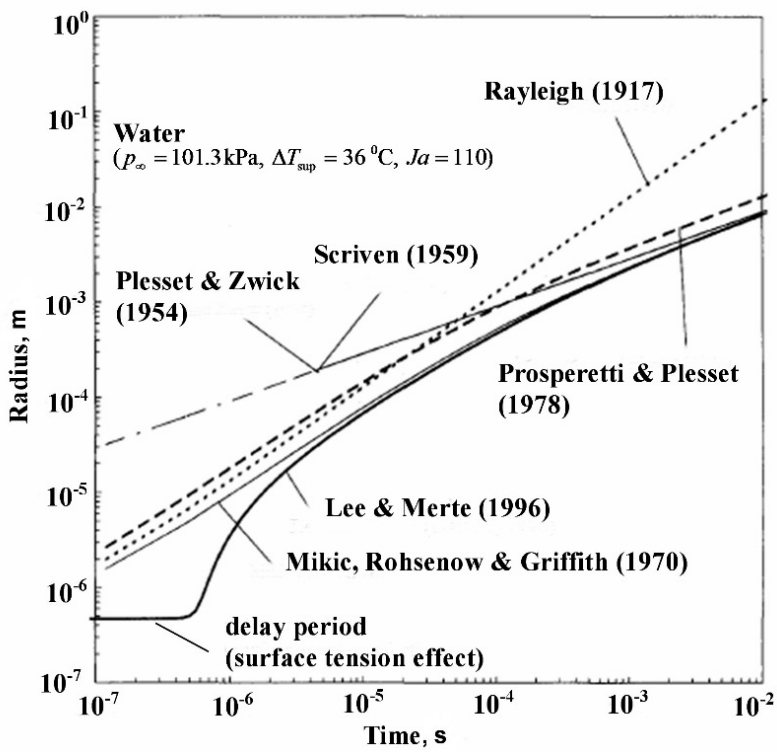

Figure 4. Comparison of bubble growth models (after Lee and Merte[6]).

Based on numerical solutions, Miyatake et al.[15] have shown that the MRG model over-predicts the bubble radius in the early stages (by up to three-fold in certain cases) primarily because it does not consider the delay period governed by surface tension effects.

5 Extensions of the MRG Model

In view of the simplicity, elegance, and reasonable accuracy of the MRG model, several extensions of this model have been proposed in order to improve the model for applicability to a wider range of conditions encountered in practical problems. The extensions are generally expressed in dimensionless form

$$R^* = f(t^*)$$

where R^*, t^* refer to dimensionless bubble radius and dimensionless time defined differently by various investigators.

Downloaded by NASA Kennedy Space Center on July 29, 2015 | http://arc.aiaa.org | DOI: 10.2514/6.2015-3952

Prosperetti and Plessset[16] proposed a scaled modified closed-form expression of the MRG model, considering a linear relation for the vapor pressure:

$$p_v(T_v) - p_\infty = \frac{p_v(T_\infty) - p_\infty}{T_\infty - T_{\text{sat}}(p_\infty)}[T_v - T_{\text{sat}}(p_\infty)] \tag{13}$$

instead of the integrated Clausius-Clapeyron equation (5c) considered in the MRG model. Theofanous and Patel[17] have shown that the assumptions in the MRG model may lead to large errors for large initial superheats, when the vapor density changes during the process significantly, and have modified MRG relation for bubble growth (to correct this deficiency) by using a more realistic dependence of vapor density on temperature. As in the MRG model, the models of Prosperetti and Plesset[16] and Theofanous and Patel[17] do not account for the delay period associated with surface tension, and the critical bubble radius.

Miyatake et al.[15] proposed a simple universal equation for bubble growth, which improves on the bubble growth expression of MRG model, so that it is valid in the surface tension, inertia, and heat diffusion controlled regions. It also accounts for bubble growth acceleration effects ($\ddot{R}$ term), which was neglected in the MRG model. The correct non-linear relationship between the vapor pressure and temperature obtained from the tabulated data eliminates the need for linear relationship considered by MRG. The recommended bubble growth equation contains parameters t_d, t_u and T_r, where the quantity t_d refers to the delay period associated with surface tension, t_u denotes the upper limit of the time period during which the bubble growth is investigated, and T_r denotes a reference temperature at which the vapor density is evaluated. Good comparisons are obtained for bubble growth in pure water and aqueous NaCl solutions. Besides the fact that the consideration of the effect of delay period is of an empirical nature, one minor limitation of this model is the use of a reference temperature T_r at which the temperature-dependent saturation density of the vapor ρ_v is evaluated. The introduction of the reference temperature calls for an upper limit of the overall time period being considered for bubble growth t_u, which is rather difficult to specify a priori.

B. Model Development

The model proposed in the present work considers an extension of the MRG model for bubble growth in an unbounded medium with a uniform superheat. The model extensions account for the delay period and the finite initial bubble radius associated with surface tension effects. Following the model validation with published benchmark test data for *unbounded medium with uniform superheat*, the model is extended to investigate *flashing liquid jets* and validated with existing water jet test data.

1. Bubble Growth in an Unbounded Medium

The present model available on request to approved agencies (ITAR and proprietary protected), in extending the MRG model[14] for bubble growth in unbounded medium takes into account the surface tension effects that are excluded in the MRG model. Thus the present model includes the effects of surface tension, inertia and heat-diffusion, but neglects viscosity effect. In order to account for the initial delay period signifying the role of surface tension and equilibrium bubble radius, the bubble growth equation is expressed in transformed variables.

The main improvements in the present model relative to the MRG model are as follows. The initial bubble radius is finite instead of zero, and corresponds to the critical bubble radius R_c, as demanded by the thermodynamics stability considerations, see Eq. (4d). The effect of surface tension is taken into account by introducing an appropriate delay period t_d during which the bubble growth is extremely small on account of surface tension of the liquid. The actual vapor pressure curve (from tabulated data) is utilized to evaluate the vapor pressure.

2 Model for Liquid Jets

The model proposed in the foregoing section for bubble growth in a uniformly superheated unbounded medium is now appropriately modified for the characterization of liquid jet flashing under superheated conditions. Fig. 5 shows a schematic of the cross sectional view of a liquid stream in vacuum, as first discussed by Muntz and Orme[4].

Downloaded by NASA Kennedy Space Center on July 29, 2015 | http://arc.aiaa.org | DOI: 10.2514/6.2015-3952

Downloaded by NASA Kennedy Space Center on July 29, 2015 | http://arc.aiaa.org | DOI: 10.2514/6.2015-3952

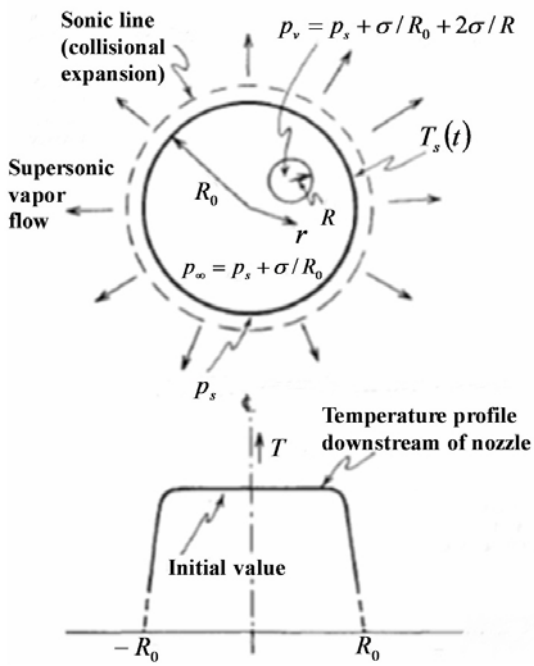

Figure 5. Bubble growth in a superheated cylindrical liquid jet (after Munoz and Orme[4]).

The following physical assumptions are made in the analysis.

1. The flow is steady.
2. The velocity and temperature of the jet are uniform in the radial direction.
3. Bubble nucleation is initiated immediately after exit from the nozzle/orifice.

a JET SURFACE TEMPERATURE

In extending the model for unbounded medium to circular jets, we need to take into account of the surface tension at the *jet surface* for obtaining the liquid pressure p_∞ far from the bubble (Muntz and Orme[4]):

$$p_\infty = p_s + (\sigma / R_0) \tag{14a}$$

where R_0 is the (local) jet radius, and p_s is the vapor pressure at the surface of the jet

$$p_s = p_v(T_s) \tag{14b}$$

which depends on the surface temperature of the jet T_s. Thus for a vapor bubble to exist or grow, the internal liquid pressure must at least be

$$p_\infty = p_s + \sigma / R_0 + 2\sigma / R \tag{14c}$$

where R is the bubble radius.

Assuming a semi-infinite slab, Schlutz and Jones[18] derived a solution for the surface temperature $T_s(t)$ of the jet exposed to vacuum as (Fuchs and Legge[1])

$$T_0 - T_s(t) = (\pi \alpha_f \rho_f c_f)^{-1/2} \int_0^t \frac{q(t')}{(t-t')^{1/2}} dt' \tag{15}$$

where T_0 is the jet initial temperature. The time-dependent surface heat transfer due to evaporation $q(t)$ is expressed by (Fuchs and Legge[1])

$$q(t) = \dot{m}_g h_{fg} \tag{16a}$$

where the mass transfer rate $\dot{m}_g$ is described by

$$\dot{m}_g = p_s / \sqrt{2\pi(\overline{R}/M)T_s} \tag{16b}$$

where $\overline{R}$ is the universal gas constant, and M the molecular weight.

To circumvent (simplify) the complicated integrand in Eq. (16), Muntz and Orme[4] proposed an explicit, although approximate, expression for the jet surface temperature by assuming that the heat flux q is constant with a value prescribed at the end of the time interval t. The surface temperature is then obtained by solving the following nonlinear algebraic equation (see also Aldred et al.[19]):

$$T_0 - T_s(t) = \frac{\sqrt{4k_f t / \pi \rho_f c_f}}{k_f} q(t) \tag{17}$$

where k_f stands for the thermal conductivity of liquid.

Fig. 6 presents the surface temperature histories calculated from Eq. (18) for various values of the jet initial temperature. These results are shown to approximately represent the exact surface temperatures obtained from Eq. 16, see Muntz and Orme[4]. The jet surface temperature falls very rapidly with time.

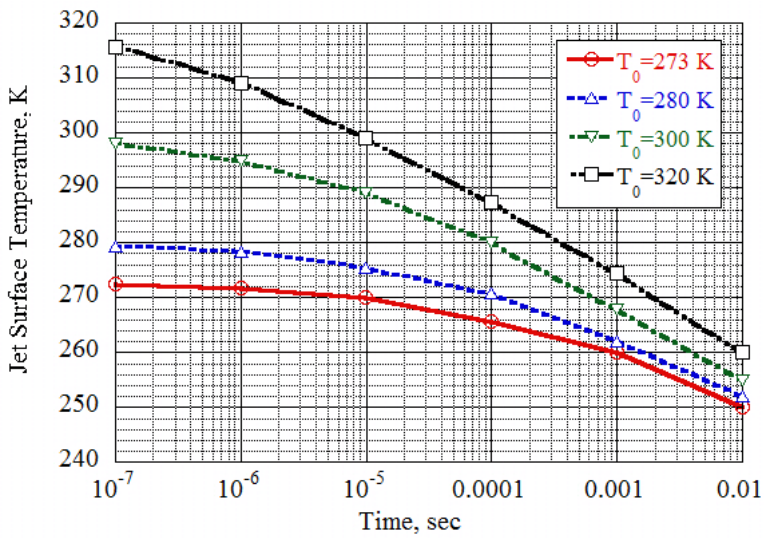

Figure 6. Jet surface temperature history due to surface evaporate.

In view of the complexity and uncertainties related to the determination of the instantaneous jet surface temperature, simplifications are introduced in the present model with regard to the estimation of *average jet surface temperature*. These simplifications are guided by the predicted jet surface temperature histories shown in Fig. 6 based on the calculations of (Muntz and Orme[4]).

b JET BURST LENGTH

There exists considerable uncertainty with regard to the jet bursting criterion. Muntz and Orme[4] assumed that jet bursting occurs when the bubble radius is equal to the local jet radius. With the help of the extended Rayleigh equation accounting for the effects of surface tension, inertia, and viscosity, Muntz and Orme[4] predicted jet bursting distances and compared them with the measurements of Fuchs and Legge[1] for water jets with various initial temperatures. The predicted bursting distances are found to be an order of magnitude lower than those of the test data.

Photographic measurements by Wildgen and Straub[20] for water jets have indicated that bubbles continue to grow up to as high as five times the size of the jet diameter before bursting takes place (Fig. 7).

Downloaded by NASA Kennedy Space Center on July 29, 2015 | http://arc.aiaa.org | DOI: 10.2514/6.2015-3952

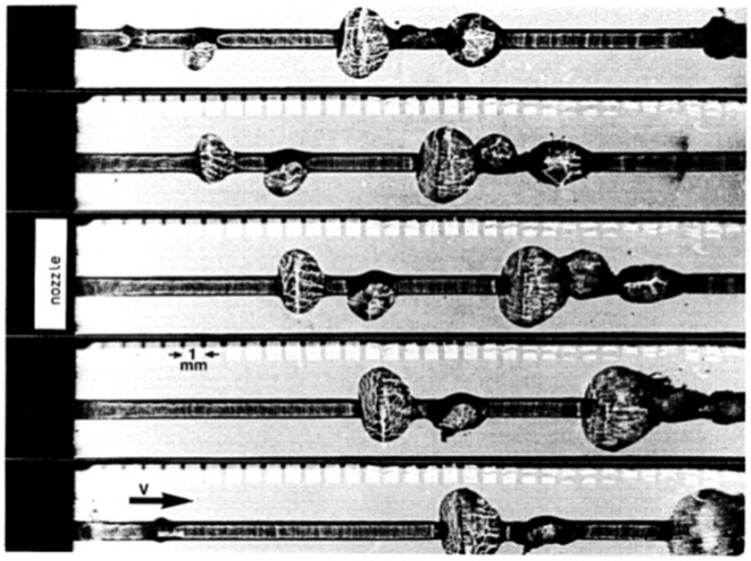

Figure 7. Criterion for jet bursting (after Wildgen and Straub[20]).

In the present model, it is considered (postulated) that jet bursting occurs when the bubble radius to jet radius exceeds a critical value of 4.

c JET CONE ANGLE

The cone angle containing majority of the droplets and frozen (ice) fragments can be obtained from (Aldred et al.[19])

$$\theta = 2\tan^{-1}\left(\dot{R}_b / V_0\right) \tag{18}$$

where $\dot{R}_b$ represents the bubble velocity perpendicular to the jet axis, taken equal to the bubble velocity (growth rate of the bubble) at the burst instant.

C. Results and Comparison

1 Bubble Growth in Unbounded Medium

a GENERAL COMPARISON WITH EXISTING MODELS

A general comparison of the predictions from the present model with the existing models for bubble growth in unbounded medium is represented in Fig. 8. The results are shown in dimensionless form, covering all the bubble growth regimes: surface tension, combined surface tension and inertia, inertia, combined inertia and heat diffusion, and heat diffusion. Models of Rayleigh[7], Plesset and Zwick[11], and Mikic, Rohsenow and Griffith[14] are considered for comparison.

Downloaded by NASA Kennedy Space Center on July 29, 2015 | http://arc.aiaa.org | DOI: 10.2514/6.2015-3952

Downloaded by NASA Kennedy Space Center on July 29, 2015 | http://arc.aiaa.org | DOI: 10.2514/6.2015-3952

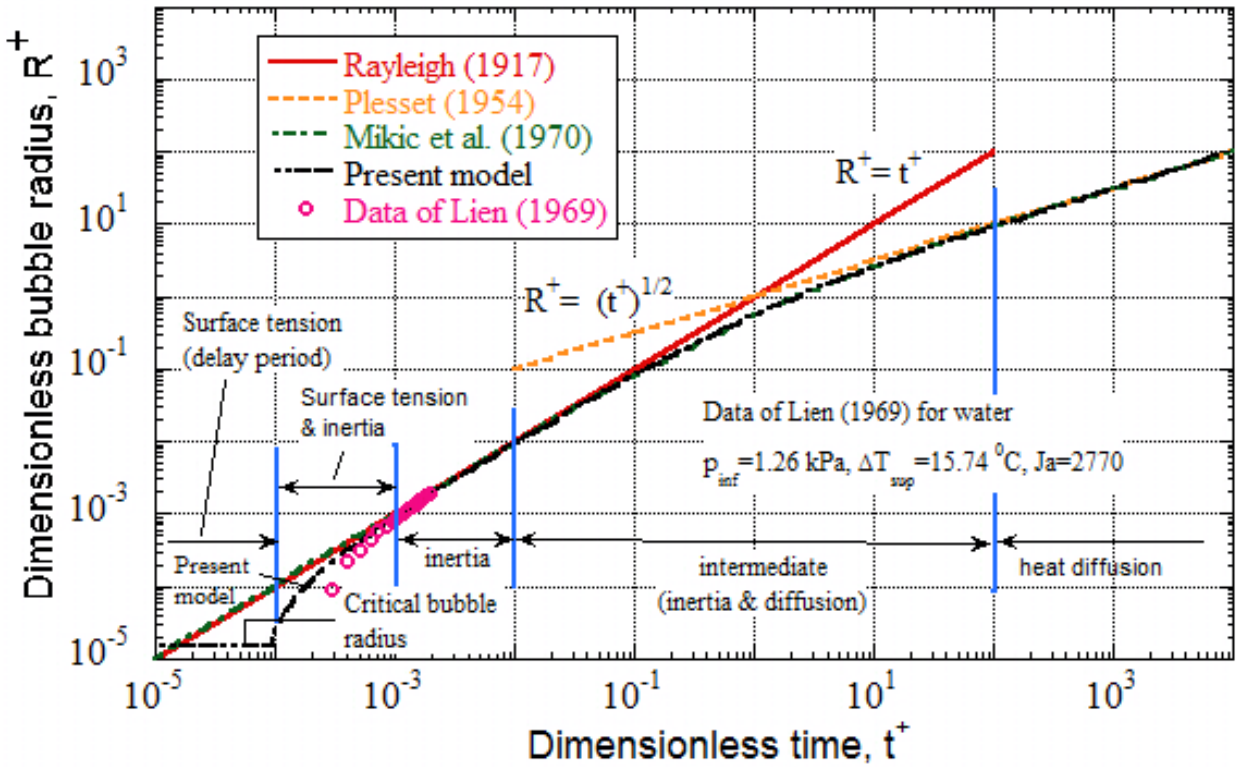

Figure 8. General comparison of bubble growth models for various regimes.

To highlight the significance of the surface tension effect and the delay period, a particular set of test data of Lien[21] are considered here: $p_\infty = 1.26\,\text{kPa}$, $T_\infty = 26.15\,^0\text{C}$, $\Delta T = 15.74\,^0\text{C}$, and $\text{Ja} = 2770$. The comparisons suggest that the present model shows an improvement over the MRG model in the surface tension regime ($t^+ < 10^{-3}$). For $t^+ > 10^{-3}$, the present model matches the MRG result, as is to be expected. The considerations of the critical bubble radius and the delay period due to surface tension helped improve the bubble growth predictions from the present model. The limitations of the Rayleigh and the Plesset-Zwick solutions are evident.

b DATA OF DERGARABEDIAN[22]

Fig. 9 shows a comparison of the bubble growth predicted by the present model with the experimental data of Dergarabedian[22] for uniformly superheated water. The test conditions considered here are $p_\infty = 0.1035\text{MPa}$, $T_\infty = 376.25\,\text{K}$, $\Delta T = 3.1\,\text{K}$, and $\text{Ja} = 9.9$. The estimated critical bubble radius $R_c = 8.0\mu\text{m}$, and the delay period $t_d = 0.018$ ms, which is small compared to the measurement time of 14 ms. The value of t^+ =115 for $t = 1$ ms, so that the data correspond to diffusion-controlled regime. It is seen that the present model describes well the bubble growth during the entire period. The MRG model also agrees with the data. On the other hand, the Rayleigh model considerably over-predicts the bubble growth, as it is applicable only in the inertia controlled regime, and loses its validity in the heat diffusion controlled regime.

Downloaded by NASA Kennedy Space Center on July 29, 2015 | http://arc.aiaa.org | DOI: 10.2514/6.2015-3952

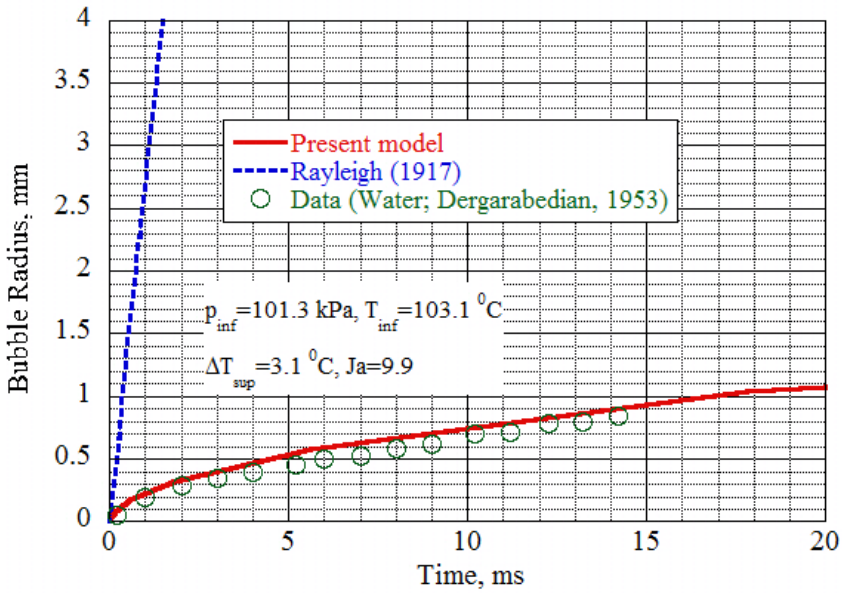

Figure 9. Comparison with the bubble growth data of Dergarabedian[22].

c DATA OF LIEN[21]

In Fig. 10, we compare the present predictions of bubble growth with the measurements of Lien[21] for water at various sub-atmospheric pressure levels and liquid superheats.

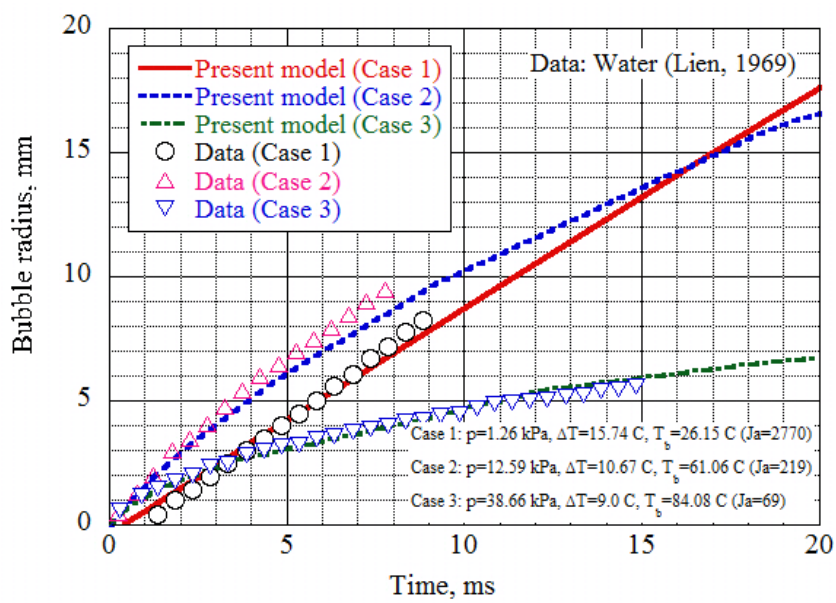

Figure 10. Comparison with the bubble growth data of Lien[21].

Three specific cases (conditions) are shown:

Case 1: $p_\infty = 12.59\,\text{kPa}$, $T_\infty = 61.06\,^0\text{C}$, $\Delta T = 10.67\,^0\text{C}$, $\text{Ja} = 219$

Case 2: $p_\infty = 1.26\,\text{kPa}$, $T_\infty = 26.15\,^0\text{C}$, $\Delta T = 15.74\,^0\text{C}$, $\text{Ja} = 2770$

Case 3: $p_\infty = 38.66\,\text{kPa}$, $T_\infty = 84.08\,\text{K}$, $\Delta T = 9.0\,^0\text{C}$, $\text{Ja} = 69$

Note that the data of Case 2 correspond to the data presented in Fig. 8. The estimated critical bubble radii for Cases 1, 2, and 3 are respectively 12.9, 6.6, and 6.2 μm. The corresponding delay times are respectively 0.037, 0.42 and 0.12 ms, which are small compared to the overall bubble growth measurement times ranging from 8 (Case 2) to 15 ms (Case 3). Note that the values of t^+ at $t = 1$ ms are 0.00022, 0.154 and 100 for Cases 1, 2, and 3 respectively. Both the data and the model (Fig. 10) suggest that the bubble growth in Case 1 is controlled by inertia (evidenced by a linear variation of bubble radius with time), whereas in Cases 2 and 3 the bubble growth quickly becomes heat-diffusion controlled. The comparisons suggest that the model satisfactorily predicts the bubble growth in all the three sets of Lien's data. The MRG model also agrees with the test data.

It is evident from the foregoing comparisons that the present model, representing an extension of the MRG model, is able to describe the bubble growth in an unbounded medium (uniformly superheated) under a wide range of system pressure and liquid superheat. The comparisons also reveal that the delay period incorporated in the present model is able to satisfactorily characterize the early growth period dominated by surface tension.

2 *Flashing Liquid Jets*

Very few data exist in the literature for flashing liquid jets. Four sets of existing data on flashing water jets are considered for comparison and validation of the proposed model. In particular, the data of Fuchs and Legge[1] and of Mann and Stoll[23] consider convergent nozzles in a vacuum chamber, the data of Kitamura et al.[24] consider a straight tube nozzle in a vacuum chamber.

a DATA OF FUCHS AND LEGGE[1]

Fuchs and Legge[1] have published photographic records of flashing jets of water discharged into a vacuum chamber with an initial pressure level of 1.33 mPa. During the venting, the pressure levels were found to be in the range of 0.133 to 66.6 Pa, depending on the jet mass flow rate. The data are obtained for various jet initial temperatures. The convergent nozzle diameter is $d_0 = 1.5$ mm, and the jet velocity is V_0 =11.8 m/s. The jet initial temperatures considered are T_0 =293 K, 313 K, and 323 K. Fig. 11 shows a photographic view of the bursting jet at jet initial temperatures of 293 K, and 313 K. Clearly, the jet bursting distance increases with a decrease in jet initial temperature.

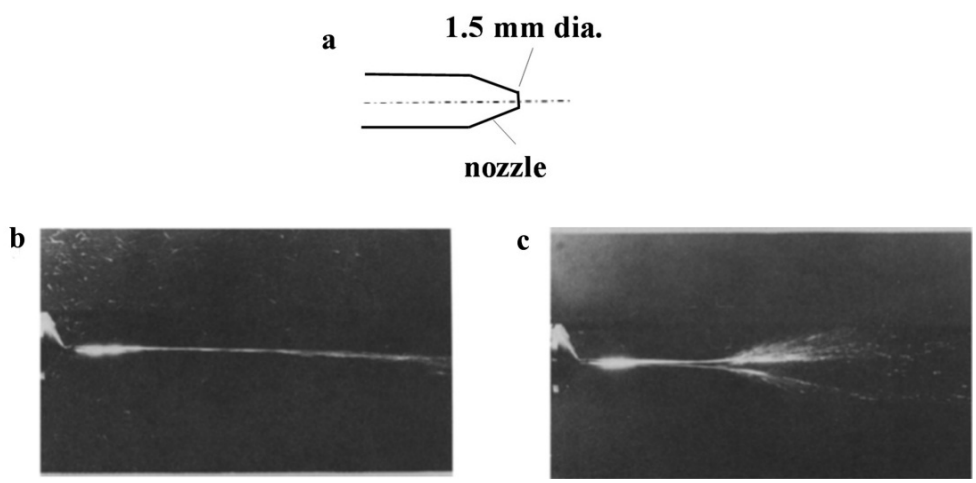

Figure 11. Photographic views of the water jet bursting (after Fuchs and Legge [1]): a) Nozzle configuration, b) T_0 = 293 K, c) T_0 = 313 K.

At T_0 =293 K, 313 K, and 323 K, the estimated liquid superheats ΔT_{sup} are 10, 20, and 25 K respectively, and the corresponding Jacob numbers *Ja* are 1820, 1985, and 1866 respectively. The corresponding critical bubble radii are 144, 25.8, and 15 μm respectively, and the delay periods are 1.18, 0.47, and 0.11 ms respectively. The predicted bubble growth for the conditions corresponding to the data of Fuchs and Legge[1] are depicted in Fig. 12.

Downloaded by NASA Kennedy Space Center on July 29, 2015 | http://arc.aiaa.org | DOI: 10.2514/6.2015-3952

Downloaded by NASA Kennedy Space Center on July 29, 2015 | http://arc.aiaa.org | DOI: 10.2514/6.2015-3952

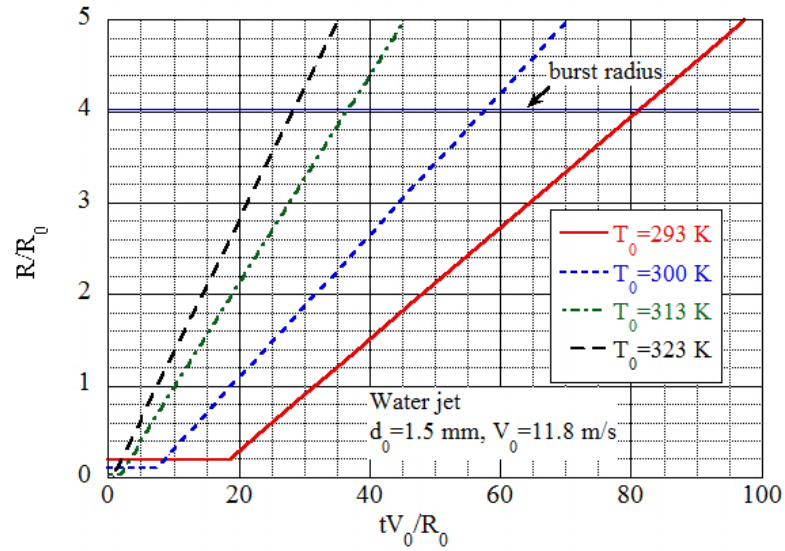

Figure 12. Predictions of bubble growth for the data of Fuchs and Legge[1].

The curve corresponding to the jet temperature of 300 K has been added, even though no data exists for that temperature. It is clear that the initial delay period increases with a decrease in the jet initial temperature. The jet bursting distance L_b is deduced from this plot in accordance with Eq. (20b). The critical bubble radius R_c / R_0 is seen to range from 0.1 at 323 K to 0.2 at 293 K. Calculations show that the time of burst t_b =5.1, 3.7, 2.3 and 1.8 ms at jet temperatures of 293 K, 300 K, 313, and 323 K respectively. The corresponding values of t_b^+ are 1.6x10^{-3}, 1.5x10^{-3}, 2.0x10^{-3} and 2.9x10^{-3} respectively, indicating the importance of surface tension and inertia effects.

In Fig. 13, we present a comparison of the bursting distance predictions with test data for various jet initial temperatures at a constant jet velocity V_0 = 11.8 m/s. Also shown are the predictions of Muntz and Orme[4] based on the extended Rayleigh model without considering heat diffusion effects, and the criterion $R_b = R_0$.

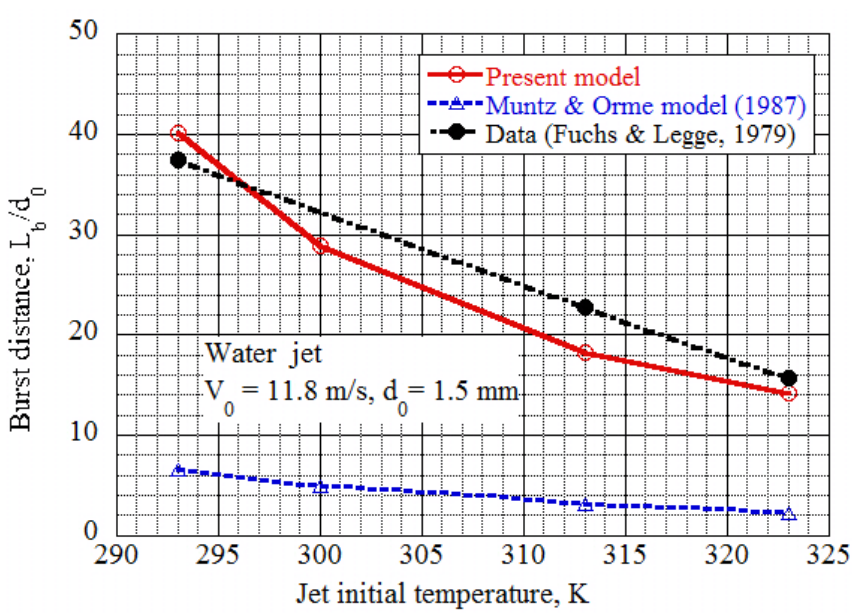

Figure 13. Comparison of jet bursting distance with the data of Fuchs and Legge[1].

The comparisons suggest that the present model satisfactorily predicts the bursting distances, and show a substantial improvement over the Muntz and Orme model[4], which under-predicts the data by roughly an order of magnitude. Both the data and the present model indicate that at a constant jet velocity, the jet burst distance increases with a decrease in jet initial temperature. The consideration of the delay period and the improved jet burst criterion afforded the improved predictions of the present model relative that of Muntz and Orme[4]. The effect of jet velocity on the burst distance at a constant jet initial temperature, as predicted by the present model, is highlighted in Fig. 14. At a given jet temperature, the burst distance increases with increasing jet velocity, as is to be expected.

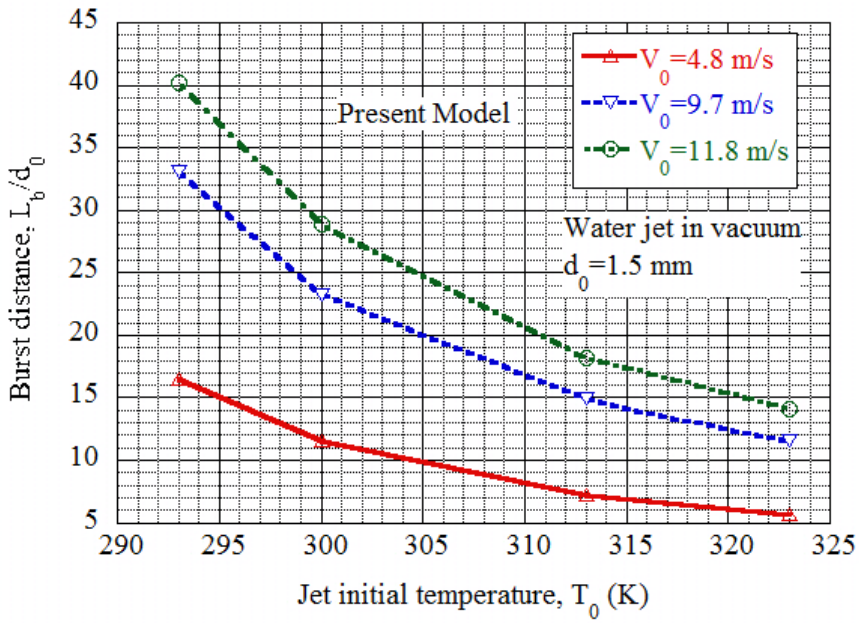

Figure 14. Comparisons of predicted velocity and temperature effects on jet burst length.

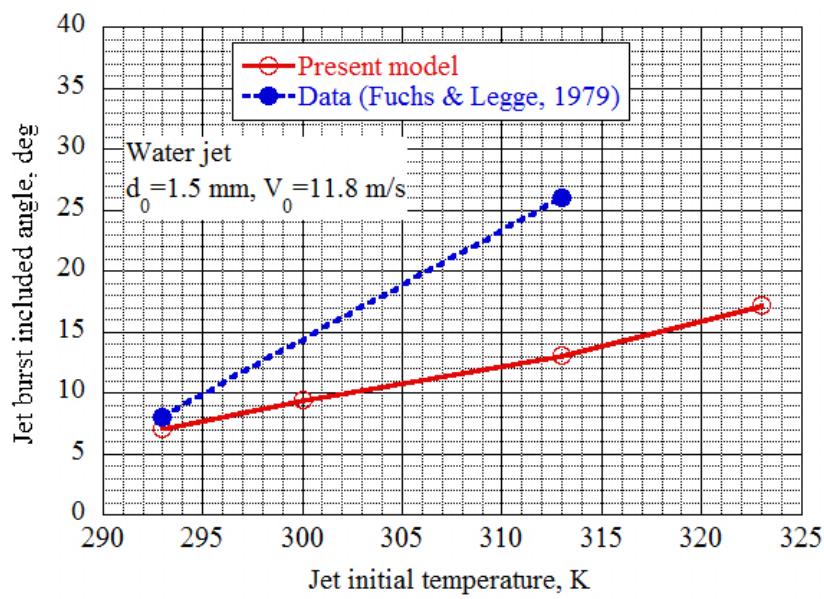

Figure 15. Comparisons of burst angle with the data of Fuchs and Legge[1].

Fig. 15 shows a comparison of the predicted jet burst included (cone) angle with the data of Fuchs and Legge[1]. At a jet temperature of 293 K, the model predicts a cone angle of about 7 degrees, which is very close to the

Downloaded by NASA Kennedy Space Center on July 29, 2015 | http://arc.aiaa.org | DOI: 10.2514/6.2015-3952

measured value of about 8 deg. But the model increasingly under-predicts the jet angle as the initial temperature is increased. It is believed that the under-prediction is partly due to the formation of a vapor-droplet cloud surrounding the flashed liquid jet, which is somewhat difficult to quantify. Steddum et al.[25] points out the problems associated with photographic determination of the cone angles of sprays. The sprays are dense near the jet centerline, and become progressively less dense away from the axis of the jet, with no clear boundary existing at the edge of the jet. Mikatarian and Anderson[26] report difficulties in determining the degree of expansion of the liquid portion of the jet on account of the presence of gaseous vapors that completely surround the liquid.

The effect of jet velocity on the predicted burst angle at a constant jet initial temperature is demonstrated in Fig. 16. It is seen that at a constant jet temperature, the burst angle increases with a decrease in jet velocity, as is to be expected. The incremental jet burst length due to changes in jet velocity increases somewhat with an increasing jet initial temperature.

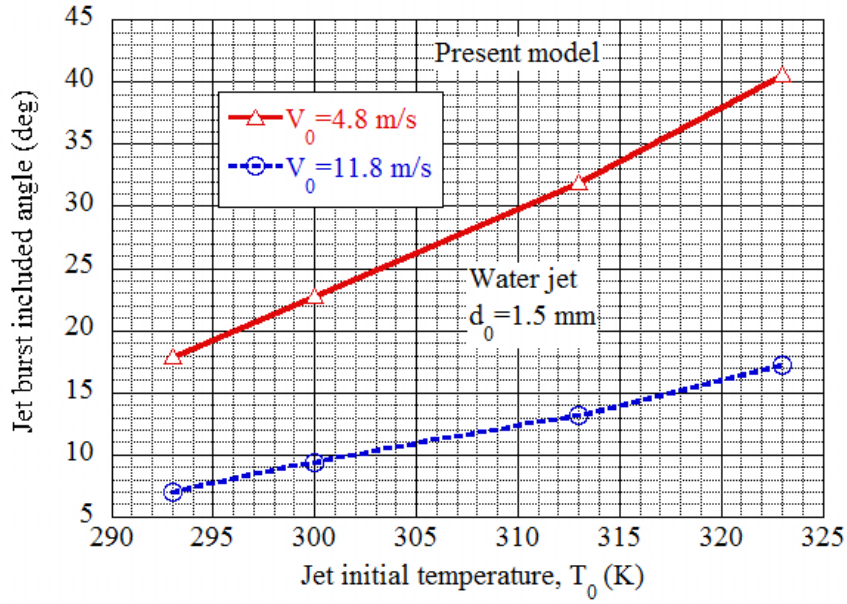

Figure 16. Comparisons of predicted velocity and temperature effects on jet burst length.

b DATA OF MANN AND STOLL[23]

Mann and Stoll[23] carried out measurements of flashing water jets issuing from a convergent nozzle and discharged into a vacuum chamber (Fig. 17). The available photographic views of the jet for jet temperatures of 294.3 K and 324.8 K are also shown. The nozzle diameter d_0 =1.397 mm, and the jet velocity V_0 =15.24 m/s. The ambient pressure p_∞ =345 Pa, corresponding to a saturation temperature of T_{sat} = 267 K. The jet initial temperatures T_0 of 282 K, 294.3 K, and 324.8 K are considered. The corresponding estimated superheats are 4.5 K, 10.6 K, and 25.9 K respectively, and the corresponding Jacob numbers are 1177, 1864, and 1864 respectively.

The estimated critical bubble radii are 738, 126 and 12.8 μm respectively, and the corresponding delay times are 11, 0.98, and 0.042 ms respectively. Calculations show that the time of burst t_b =7.9, 4.5 and 1.6 ms at jet temperatures of 282 K, 294.3 K, and 324.8 K respectively. The corresponding values of t_b^+ are 1.9x10^{-3}, 1.45x10^{-3}, and 2.8x10^{-3} respectively, indicating the importance of surface tension and inertia effects. Fig. 18 shows the predicted bubble growth for the three jet initial temperatures. It is seen that the delay period at a jet temperature of 282 K is considerably large relative to those at 294 K and 325 K.

Downloaded by NASA Kennedy Space Center on July 29, 2015 | http://arc.aiaa.org | DOI: 10.2514/6.2015-3952

Downloaded by NASA Kennedy Space Center on July 29, 2015 | http://arc.aiaa.org | DOI: 10.2514/6.2015-3952

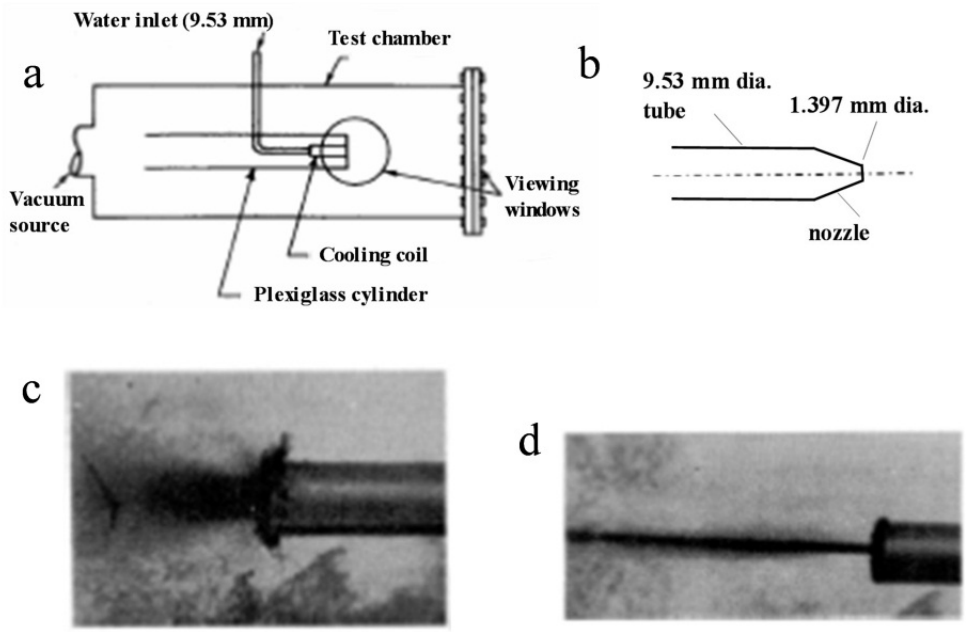

Figure 17. Flashing water jet (Mann and Stoll[23]): a) test chamber, b) nozzle configuration, c) T_0 =324.8 K, d) T_0 =294.3 K.

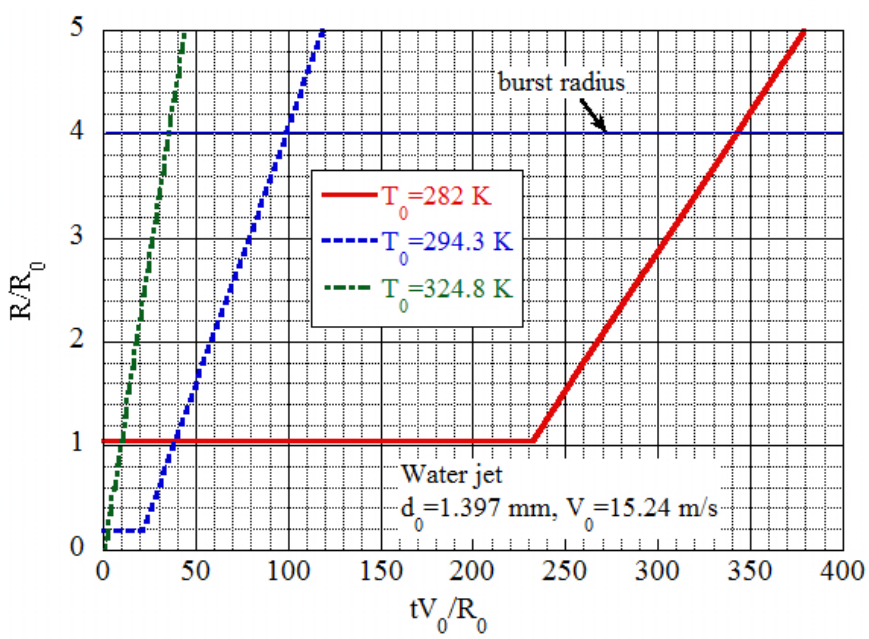

Figure 18. Predicted bubble growth for the data of Mann and Stoll[23].

Table 1 compares the predicted jet characteristics with the test data for the burst distance and the cone angle for the three jet initial temperatures considered. The predictions are seen to be representative of the measurements. It is remarkable that at the jet initial temperature of 282 K, the model predicts that the burst distance is about 173 jet diameters, which could not be observed due to limitations associated with the chamber length. Also the predicted jet

cone angle at this jet temperature is about 2 deg., whereas in the measurements only straight liquid jet is reported to be observed over the available length of the chamber.

Table 1. Comparison of predictions with the test data of Mann and Stoll[23] (V_0 =15.24 m/s, d_0 =1.397 mm, p_∞ =345 Pa, T_{sat} =267 K).

Quantity	T_0 =324.8 K		T_0 =294.3 K		T_0 =282 K	
	Model	Data	Model	Data	Model	Data
Bursting distance (jet diameters)	17.3	23	49.1	38	173.3	-*
Included cone angle (deg)	13.6	30	5.7	4	2.3	-

*No bursting of jet is observed within the available chamber length.

c DATA OF KITAMURA ET AL.[24]

Kitamura et al.[24] conducted experiments on flashing water jets issuing from a long nozzle into a vacuum chamber (Fig. 19). The nozzle diameter d_0 =0.54 mm, and a jet velocity of V_0 =8.2 m/s. The ambient (discharge) pressure p_∞ =2,730 Pa. The jet initial temperature is T_0 =342.7 K. The photographic view of the jet provides information on the jet burst location and the burst cone angle.

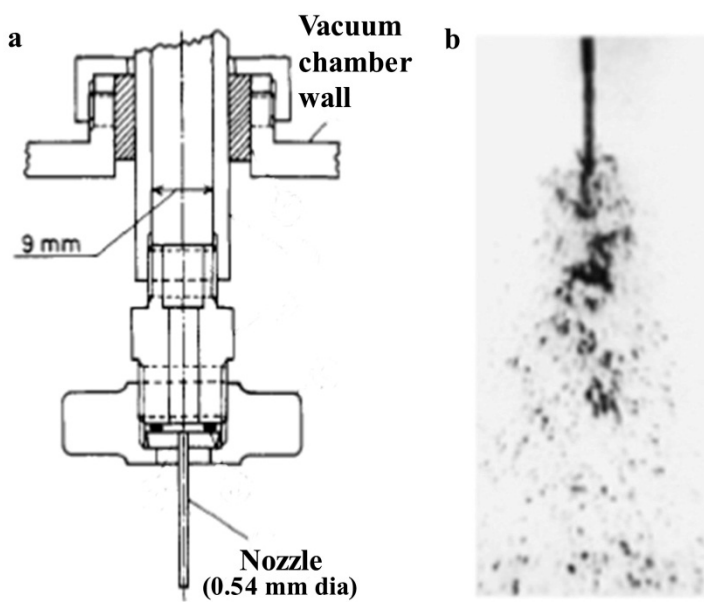

Figure 19. Breakup pattern of superheated water jet (Kitamura et al.[24]).

Fig. 20 shows the predicted bubble growth for these test conditions. The liquid superheat is 47.2 K, and the corresponding Jacob number is Ja =4,097. The critical bubble radius $R_c = 4.6\mu\text{m}$, and the delay time t_d =0.012 ms. Calculations show that the time of burst t_b =1.0 ms, and the corresponding values of $t_b^+ =$ 5.5x10^{-3}, indicating the importance of surface tension effects.

Downloaded by NASA Kennedy Space Center on July 29, 2015 | http://arc.aiaa.org | DOI: 10.2514/6.2015-3952

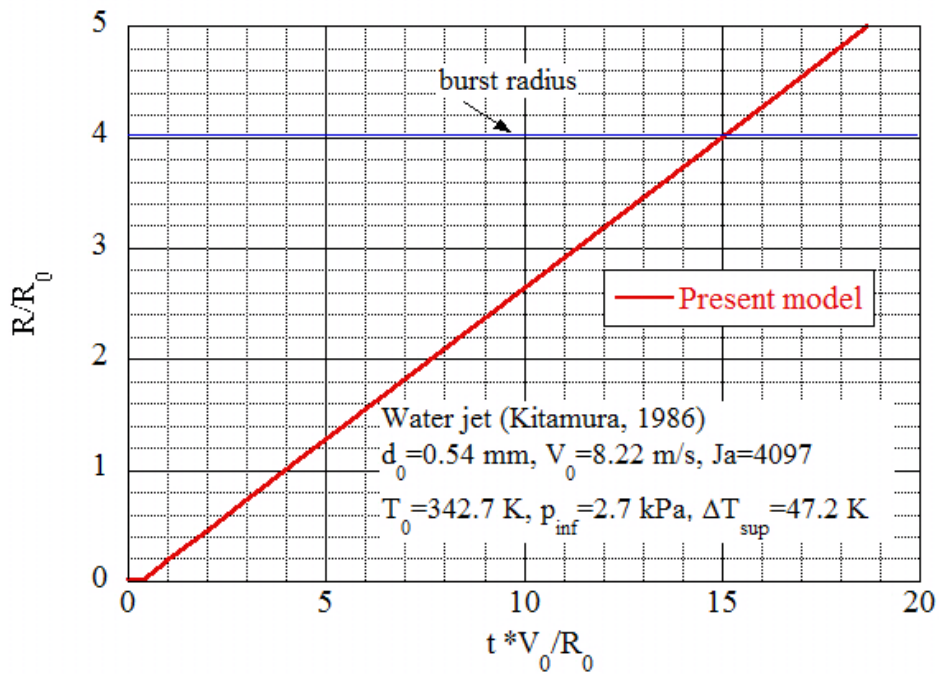

Figure 20. Predicted bubble growth for the data of Kitamura et al.[24].

Table 2 highlights a comparison of the predicted jet burst distance and burst angle with the test data. The predicted burst distance is 7.5 jet diameters, whereas the data suggest that the location of the jet disintegration is about 13 jet diameters, which is considerably larger than the predicted value. This discrepancy is perhaps connected with dynamic (vapor-liquid non-equilibrium) effects that might become important at high Jacob numbers, which tend to reduce bubble growth rates; see Griffith[27] and Cola and Shulman[28]. The predicted cone included angle is about 29.6 degrees, whereas the test data indicates an included angle of 38 degrees.

Table 2. Comparison of predictions with the test data of Kitamura et al.[24].
(V_0 =8.2 m/s, d_0 =0.54 mm, T_0 = 342.7 K, p_∞ =2,730 Pa, T_{sat} =296 K)

Quantity	Model	Data
Bursting distance (jet diameters)	7.5	13
Included cone angle (deg)	28.6	38

The burst length and the angle of dispersion are the primary focus of the venting model presented here. In addition, the droplet average size, droplet size-distribution and velocity of droplet as a result of bubble burst remain to be investigated. Roughly speaking, the size of the droplet may be scaled by the local jet diameter at the instant of bursting (Kandula[29]). Detailed experimental measurements of the jet bursting length, cone angle of dispersion, droplet size and velocity are being planned to investigate the behavior of vented jets in vacuum conditions.

D. Summary of Vent Model Development

A new bubble growth model, accounting for surface tension and initial bubble radius, was proposed that was satisfactorily validated with existing water test data for unbounded medium as well as flashing jets. The model accurately predicts that the jet burst distance increases with jet initial temperature, and decreases with a decrease in jet initial velocity. Continued validation with proposed testing for water reference and other actual intended on-orbit hypergolic fluids and nozzle configurations ("test as you fly") will strengthen the model and limit operational risks.

Downloaded by NASA Kennedy Space Center on July 29, 2015 | http://arc.aiaa.org | DOI: 10.2514/6.2015-3952

III. The Challenge of On-Orbit Propellant Mass Flow Measurement

A non-cooperative or cooperative multi-client satellite servicing system has the need for measuring commodity mass transferred to the client spacecraft with the following relevant component-level goals:

1) Accuracy: 0.5% (overall error) or better of the quantity transferred
2) Same design compatible and operable with the following commodities: N_2O_4, MMH, and N_2H_4
3) Volumetric flow rates: 0 to about 6 liters per minute (0 to about 1.5 gallons per minute)
4) Commodity temperatures: 10-50 degrees Celsius (50 to 122 degrees Fahrenheit)
5) Geosynchronous or low earth orbit operational environment
6) External load environments during launch and flight

Due to uncertainty in the bus/servicer tank design, it was decided that measurement of commodity would be achieved by integration/totalization of the observed instantaneous flow rate at the outlet of the PTA, as opposed to direct bulk storage quantity measurement (such as using Pressure-Volume-Temperature or implementing tank capacitance probes). This decision permits the development effort to be conducted at the component level rather than at an integrated system level in which instrumentation available for a client is typically limited and varies. The approach reduces the overall project risk and cost. Initial testing on leading flow meter technology candidates commenced with both a simulant (substitute) fluid and later with NTO, which represents the worst case of hypergol fluid compatibility along with implications to flow meter accuracy.

The flow meters were tested using the specific PTS parameters (namely pressure, temperature, flow rate, and transfer amount ranges). Particular parameters like K-factor, nonlinearity, pulse flow measurement, slewing rate, steady state error, and turndown ratio will not be addressed in detail in this report as they were either not tested or are not considered as key driving items in the flow meter selection for the PTS. Many of these topics are discussed in the more general flow meter test campaign by Baird[30] which included ground and microgravity testing. See Appendix A for details relevant to the present study.

A. Technology Selection

A trade study was conducted in an attempt to select primary and secondary flow meter candidate technologies for further consideration and advancement to the flight component development and qualification test phases. Fig. 21 shows the decision tree for the satellite servicing flow meter selection and the findings from the initial research to the right of each flow meter technology. The accuracy goal was considered the key factor in the trade study; heritage space flight service was considered a secondary factor as market research suggested that few, if any, commercially available technologies have actually flown in space. In anticipation of the expense associated with a redesign/qualification effort for any commercially available, high accuracy meter, an in-line flow, ultrasonic flow meter technology was selected as the primary candidate based on advertised performance and the partial qualification for space flight. A balanced-orifice flow meter was chosen as the secondary candidate based on its simplicity, availability of flight-qualified components, and historic test results. A commercially available coriolis meter was selected as the third candidate based on its observed accuracy along with serving as a tertiary standard during testing.

Five different flow meters were tested during the PTA test campaign, including one ultrasonic, three Coriolis, and one balanced orifice (as shown in Fig. 22). The flow meter reference designators shown in Fig. 22 and the corresponding meter types and advertised accuracies are listed in Table 3.

Downloaded by NASA Kennedy Space Center on July 29, 2015 | http://arc.aiaa.org | DOI: 10.2514/6.2015-3952

Downloaded by NASA Kennedy Space Center on July 29, 2015 | http://arc.aiaa.org | DOI: 10.2514/6.2015-3952

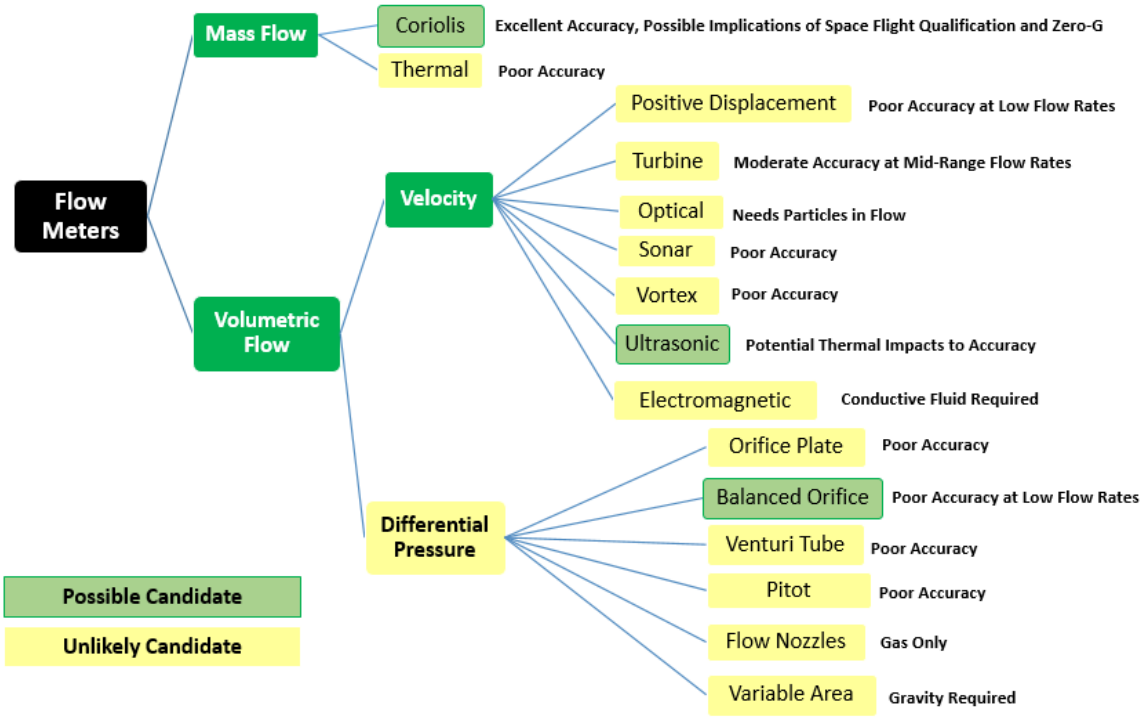

Figure 21. Flow meter trade study decision tree.

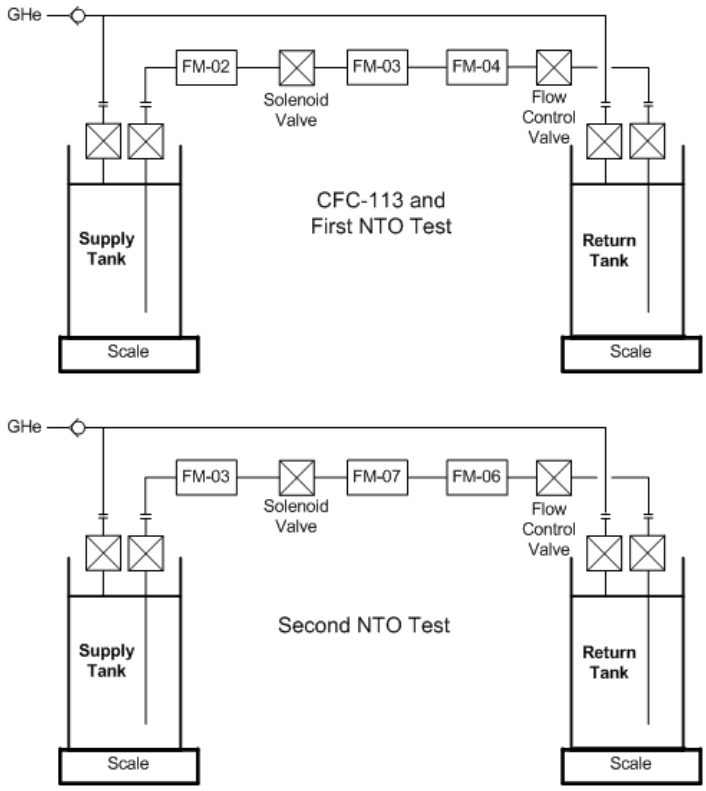

Figure 22. Simplified flow meter test setups.

Table 3. Reference designator and flow meter cross reference.

Reference Designator	Meter Type	Manufacturer Advertised Accuracy
FM-02	Ultrasonic	<0.5%
FM-03	Coriolis	<0.5%
FM-04	Balanced Orifice	<1.0%
FM-06	Coriolis	<0.5%
FM-07	Coriolis	<0.5%

The tested in-line, ultrasonic flow meter (UFM) utilizes the contra-propagating transit-time flow measurement method. A pair of ultrasonic transmitters beam signals upstream and downstream to receivers placed across a flow conduit. The flow rate is determined by the detected difference in the time of travel, which is related to the average velocity of flow in the conduit (as indicated in Fig. 23). The device that was tested sends the signals through the flow in-line with the flow direction. The meter reports in *volumetric* flow rate. It is nonintrusive, and has no moving parts, entailing minimal pressure drop. The calibration of the meter is sensitive to the nature of the fluid, and the presence of gas bubbles (even in small concentrations) can appreciably change the speed of sound (and thus the transit time) or signal attenuation. For a flight system it would be welded in-line in a seal-less configuration.

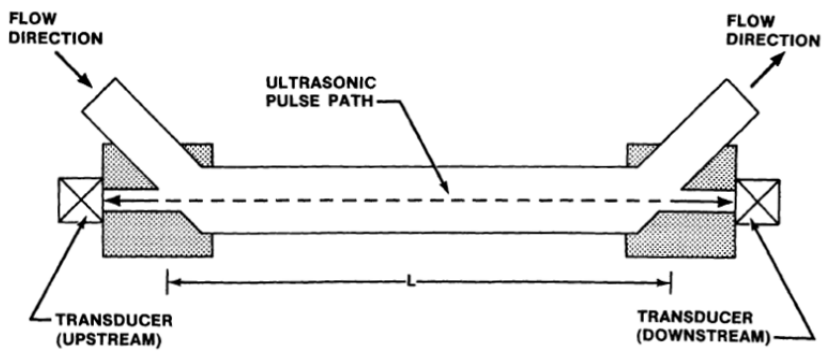

Figure 23. Notional in-line ultrasonic flow meter schematic[30].

In addition to the manufacturer's advertised performance of the UFM that was tested, additional information was obtained related to UFM's that were tested during the Space Shuttle Program for use during hypergol propellant loading and on the orbiter water coolant loop[31,32]. It was found that strap-on cross flow type UFM (notionally shown in Fig. 24) was able to achieve accuracies of 0.25 to 0.5% in a laboratory with water at flow rates in the range of 0 to 360 lb/min (0 to 30 gpm NTO). Additionally, a similar UFM was tested on the Space Shuttle Orbiter's water coolant loop floodlight coldplate with a flow rate range of about 0.08 to 0.5 lb/min (5 to 30 lb/hr) with accuracies on the order of 10% to 20% for the short duration (about 0.1 gallon) transfers[31].

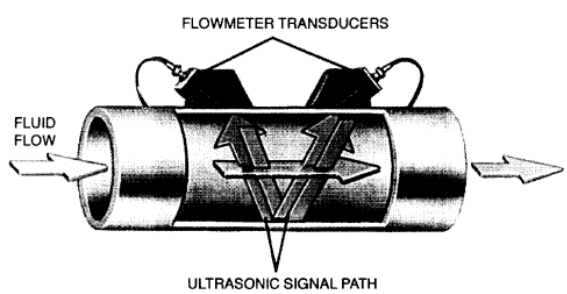

Figure 24. Strap-on UFM schematic.

Downloaded by NASA Kennedy Space Center on July 29, 2015 | http://arc.aiaa.org | DOI: 10.2514/6.2015-3952

A Coriolis flow meter functions by passing the fluid through a sensor tube with an induced natural frequency vibration perpendicular to the flow direction. The Coriolis effect introduced by the moving mass causes the tube to deform or twist which is directly proportional to the *mass* flow rate (as shown in Fig. 25). The Coriolis meter has relatively high accuracy, and can handle both single- and limited two-phase flows. A coriolis meter can also measure fluid density and temperature. There are no moving parts in the flow stream, however, the induction of the vibration requires active components that are considered intrusive in the fluid system. For a flight system it would be welded in-line in a seal-less configuration.

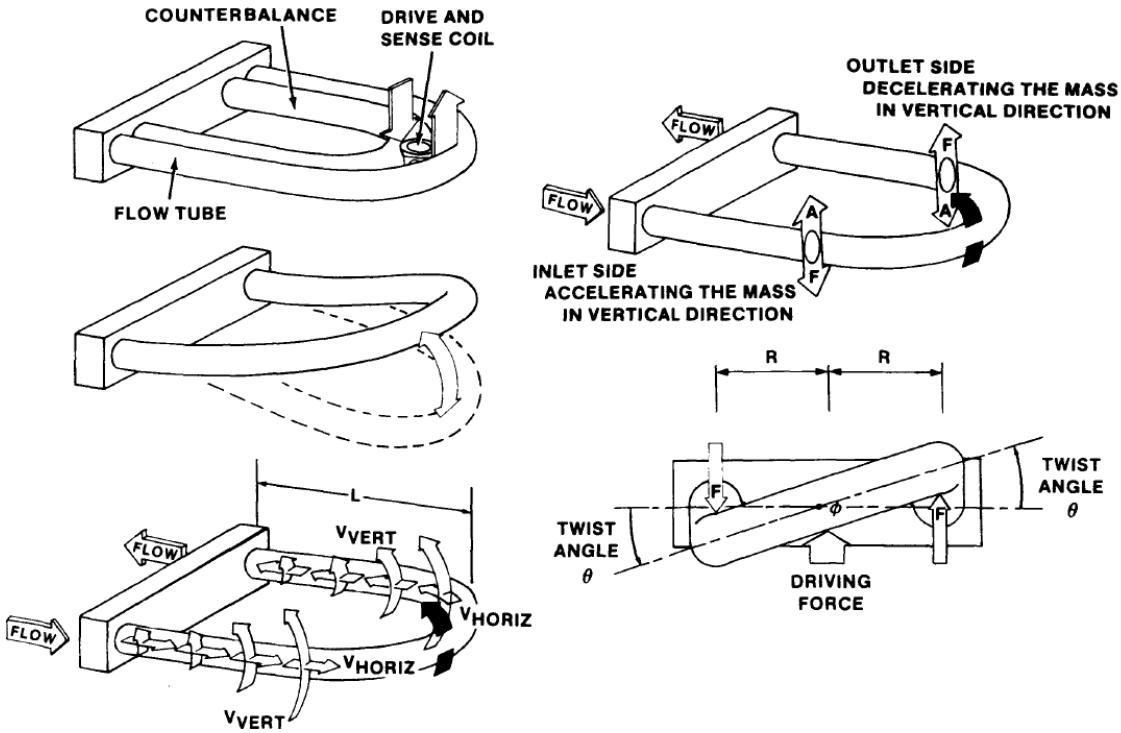

Figure 25. Notional Coriolis flow meter schematic and description[30].

An attempt was made to create a micro Coriolis flow meter that has the potential to be space-flight qualified[33]. Lotters[33] describes the development of a micro Coriolis flow meter (that was proven via testing) of measuring between 0.0008 and 0.003 lb/min (6 mg/s to 24 mg/s) with water. The intent was to use the micro Coriolis flow meter in a satellite hydrazine propulsion system[33]. The sensor shows promise, but is still in the development phase.

A balanced orifice flow meter consists of a multi-hole orifice plate inside a flow tube. Fig. 26 shows a simplified flow profile of the BFM. The multi-hole design results in lower pressure drop and quicker pressure recovery across the orifice plate as compared to a single hole orifice[34]. The *volumetric* flow rate is proportional to the square root of the differential pressure across the orifice plate (created by the constriction in the pipe or area change) in accordance with the Bernoulli principle. Mass flow rate requires the determination of fluid density. There are no moving parts, and both single- and limited two-phase flows can be measured. Much lower pressure drop is manifested and faster pressure recovery is achieved as compared to a single-hole orifice meter. The meter is fairly accurate, and established calibration methods are available. Several practical configurations has been tested in industrial and propulsion system applications[34]. Highly accurate pressure sensors are required for implementation if high flow rate accuracy is required. The meter is not suitable for pulsating flow. There are known limitations at low flow rates based on physics (pressure drop asymptotically approaches zero as the flow rate decreases). A flight BFM is considered non-intrusive since it is simply an orifice with tubing routed to a pressure transducer on each side to measure the pressure drop. For a flight system it would be welded in-line in a seal-less configuration.

Downloaded by NASA Kennedy Space Center on July 29, 2015 | http://arc.aiaa.org | DOI: 10.2514/6.2015-3952

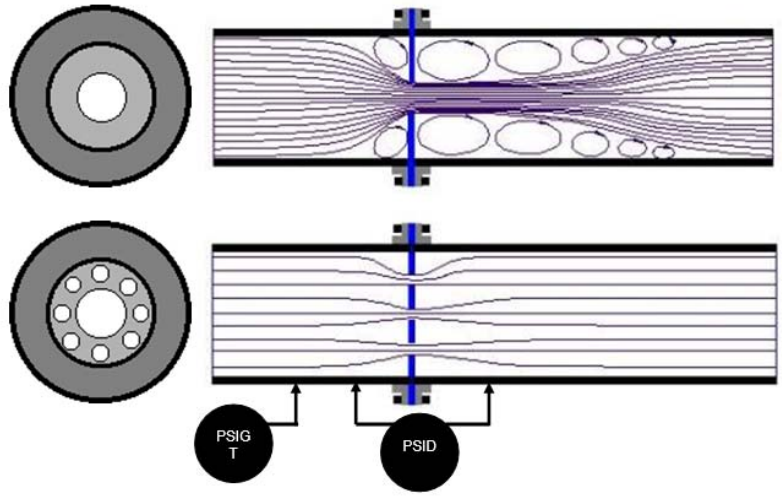

Figure 26. Simplified flow profile of a balanced orifice flow meter (shown in lower figure)[34].

B. Test Plan and Implementation

A test matrix was developed based on the expected propellant servicing concept of operations. The majority of the planned flow meter tests were to determine the totalized accuracy with respect to various transfer amounts. Flow rates were varied to determine the respective meter's sensitivity to this parameter. A limited capability to thermally condition the fluid was added to evaluate sensitivities to thermal effects up to about 120 degrees F.

Fig. 22 shows a simplified notional test setup. In each transfer test run, the fluid from the supply tank passed through various flow meters before entering the receiver/return tank. A flow control valve was positioned upstream of the return tank. The flow meters were situated upstream or downstream of the solenoid isolation valve, which controlled the flow initiation and termination. The supply tank was not pressure regulated, and the return tank was compressively filled. The tanks were isolated from vent and pressure sources during the fluid transfer so that corrections due to the addition or discharge of ullage gas or propellant vapor mass were not required.

Digital precision scales placed under the supply and the return tanks served as standards, with the supply tank scale considered the primary standard (with accuracy of less than 0.1%). The scales were functionally checked with known calibrated Class F weight standards prior to and after use. The flow meter accuracy was calculated from the following relation:

$$\%\ \text{Accuracy} = \frac{(\text{Flow meter totalized mass} - \text{Scale transfer mass})}{\text{Scale transfer mass}} \times 100$$

where the scale transfer mass represents the difference between the scale starting and final readings. A negative sign was added to the value of the return scale transfer mass for consistency.

A mass totalizer was integrated into the control and data recording system. The control and data recording system auto-sequencer controlled the solenoid isolation valve based upon a preset transfer amount. The data rate was varied for finer sampling rates for first 10 seconds followed by lesser rates for steady state flow in the interest of minimizing the bulk quantity of data. When 99% of target mass was reached, the sampling rate was changed back to finer rates and remained until 10 seconds after the solenoid valve was closed. The mass totalizer start and stop times were based on predetermined threshold flow rate level for each flow meter.

Fluid temperature conditioning was implemented by an in-line heat exchanger that was situated between the supply tank and the test assembly inlet. Constant mass flow rate was maintained (typically within 0.03 lbs/min or better as seen in Fig. 27) by pumps (with variable pump speed controlled by software) and by needle flow control valves (manually controlled).

Recorded flow parameters included meter flow rates, pressure (line pressures and tank pressures), temperatures, scale mass indications, and solenoid valve positions.

Downloaded by NASA Kennedy Space Center on July 29, 2015 | http://arc.aiaa.org | DOI: 10.2514/6.2015-3952

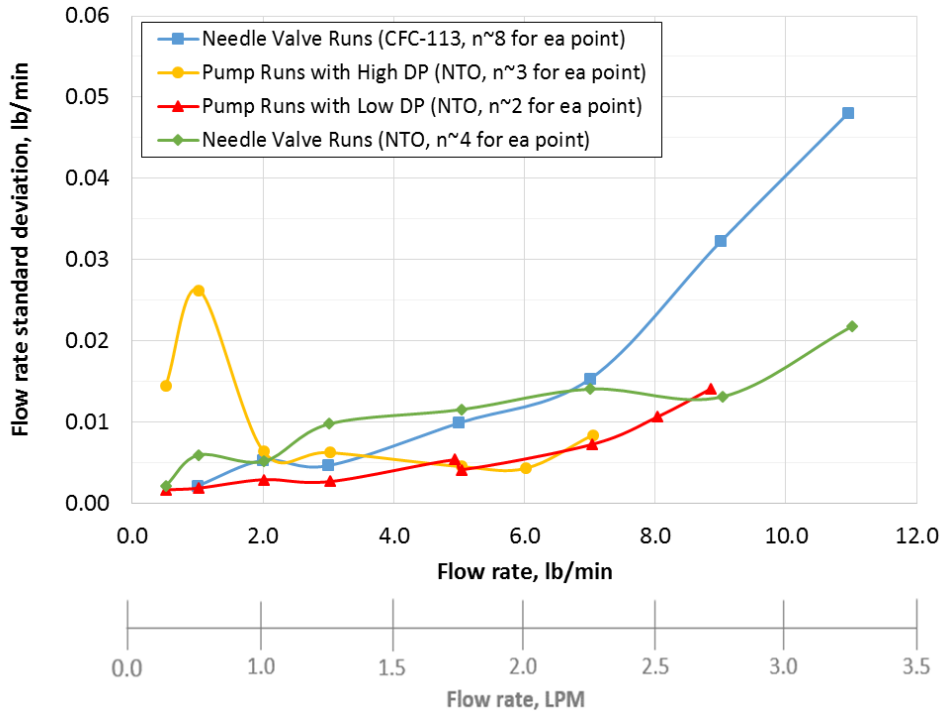

Figure 27. Comparison of flow rate control via needle flow control valves and pump RPM feedback control.

The meters were tested using CFC-113 (an adequate simulant fluid for NTO). Additionally, the decision was made to evaluate meter performance using what was considered the most challenging of the flight fluid commodities - Nitrogen tetroxide (NTO) - via actual test. The basic concepts of the technologies selected suggested that the meters would be largely insensitive to the spacecraft fluids; however, certain system properties were found to influence the flow meter reading, some of which will be discussed in greater detail.

C. UFM Tests

1 UFM Setup: Tuning, Calibration, and Data Processing

Various implementations of ultrasonic flow meter technology exist, however, the in-line UFM was selected primarily based on the fact it was advertised as partially qualified for space flight. Additionally, the meter volumetric flow rate calibration was advertised to be "medium independent", allowing use with multiple commodities without adjustment or correction other than initial "tuning."

a UFM Tuning

"Tuning" is a process that entails adjusting the meter signal processing unit timing and sensitivity based on the speed of the sound and acoustic attenuation properties of the fluid. It must be completed before the meter will produce a signal. In this program, the adjustment was done manually, and could only be performed after the meter tube was filled with fluid. For a flight application, tuning would either have to be reliably pre-set prior to system activation, or some implementation of remote real-time adjustability would be required.

b UFM Calibration and Data Processing

The UFM unit that was tested output in instantaneous flow rate. Some previous implementations had integrated totalizers built into the unit. It was calibrated at the manufacturer facility using a water piston prover and scale. The mass flow rate was referenced to catch and weigh data. The delivered manufacturer calibration data listed both volumetric and mass flow rates. The volumetric flow rate was derived from the mass flow rate using the density of water.

After testing began with CFC, the meter displayed a fairly repeatable offset at zero flow conditions that was not reflected in the water calibration curve.

Downloaded by NASA Kennedy Space Center on July 29, 2015 | http://arc.aiaa.org | DOI: 10.2514/6.2015-3952

Downloaded by NASA Kennedy Space Center on July 29, 2015 | http://arc.aiaa.org | DOI: 10.2514/6.2015-3952

2 UFM Test Results

Testing of the UFM was performed with both CFC-113 and nitrogen tetroxide (NTO). Detailed results are discussed in the following sections.

a UFM CFC-113 TEST RESULTS

The largest data set was gathered during the CFC-113 test series. Fig. 28 shows UFM accuracy in comparison with the small scale (calibrated primary standard) for ambient pressure-fed transfers of various flow rates with CFC-113. This combined data set includes transfers of 11, 22, 44, 143, 187, and 309 lbs.

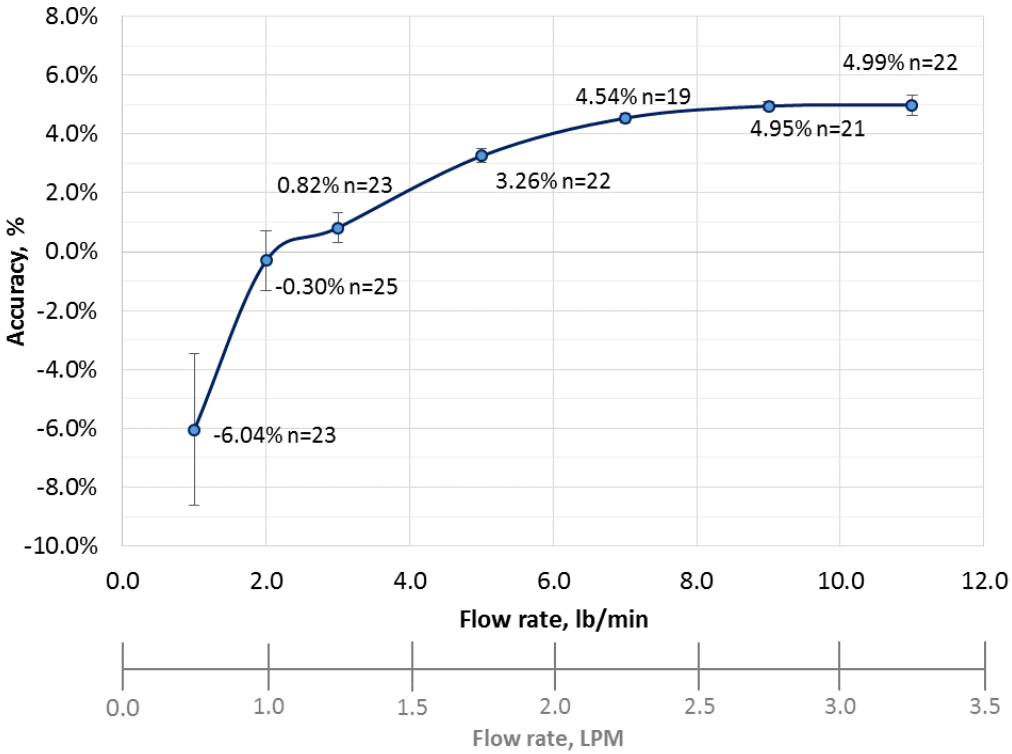

Figure 28. UFM test data, CFC-113 ambient temperature, pressure transfers.

Table 4. UFM test data, CFC-113 ambient pressure transfers.

Number of Runs (n)	Flow Rate (lb/min)	Average UFM Accuracy	UFM Standard Deviation
23	1	-6.04%	2.57%
25	2	-0.30%	1.00%
21	3	0.82%	0.50%
22	5	3.26%	0.24%
19	7	4.54%	0.16%
21	9	4.95%	0.14%
22	11	4.99%	0.34%

Total=153

The accuracy of the UFM was found to be a function of the flow rate and not of the transfer amount Table 4 lists UFM accuracy data with the standard deviation for each flow rate for the CFC-113 ambient temperature pressure-fed transfers. The standard deviation (repeatability) of the unit at lower flow rates was fairly significant and

in some cases wider than the accuracy goal of 0.5% for the unit. Due to the relatively large variation in standard deviation at low flow rates, these runs were given extra scrutiny.

The UFM displays a unique characteristic at higher flow rates (5 lb/min or higher). Due to the relatively large variation in accuracy (standard deviation) at low flow rates, these runs were given extra scrutiny. Since the Coriolis flow meter also generates instantaneous flow rate, the Coriolis flow rate data was compared to the UFM flow rate data over these flows. For the purpose of data presentation, the UFM flow rate was normalized to the Coriolis flow rate. The "UFM normalized flow rate" is defined by the following equation:

$$UFM\ normalized\ \ flow\,rate = \frac{UFM\ instantaneous\ \ flow\,rate}{Coriolis\ instantaneous\ \ flow\,rate}$$

The normalized flow rate was then plotted against the normalized mass transfer. The "normalized mass transfer" is defined by the following equation:

$$Normalized\ mass\,transfer = \frac{Instantaneous\ mass\,transferred\ based\ on\,Coriolis\ \ flow\,meter\ totalizer}{Total\ mass\,transfer\ \ for\,the\,test\,run\,based\ on\,Coriolis\ meter}$$

It was observed that at low flow rates, the UFM exhibited a flow rate decrease anomaly for some runs. Fig. 29 shows a typical example of this anomaly. It is unclear why the flow rate decrease occurred. Temperature effects were generally ruled out as the test laboratory was a temperature controlled environment so the variation should be comparatively small.

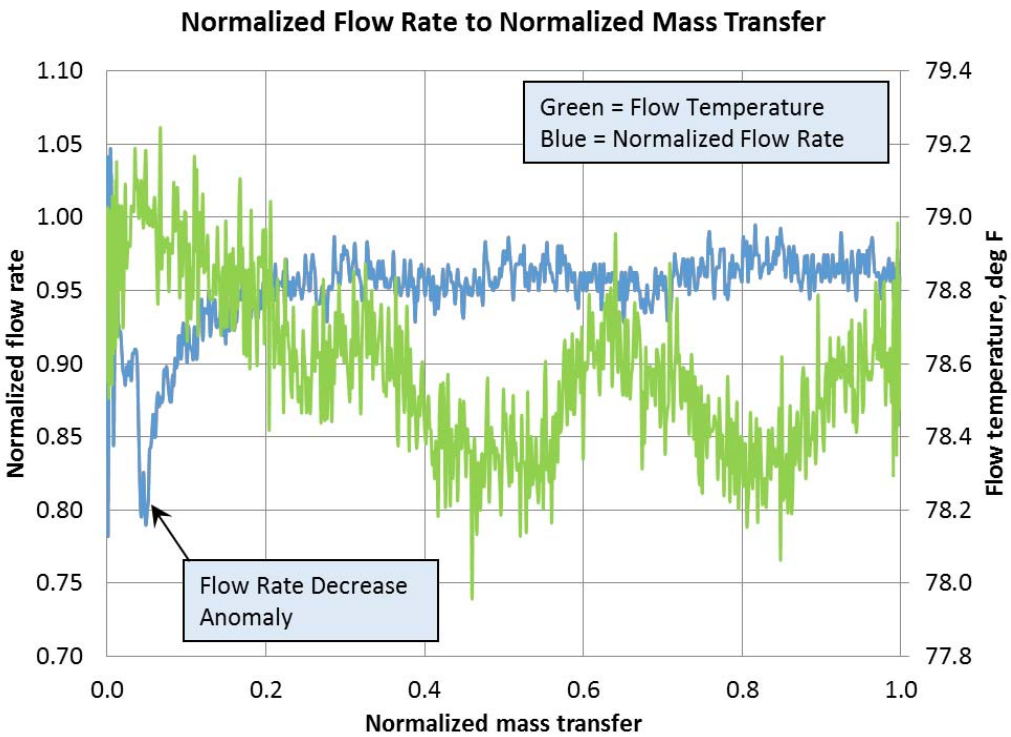

Figure 29. Example of UFM flow rate decrease anomaly.

For heated testing, the resulting flow meter accuracy varied widely, despite efforts that maintained the sounding units at the same temperature (vendor recommended practice). Fig. 30 shows data from a heated CFC-113 transfer. Due to the limited sample set, it is difficult to make a quantitative assessment; however, in general, the following trends were noted:

Downloaded by NASA Kennedy Space Center on July 29, 2015 | http://arc.aiaa.org | DOI: 10.2514/6.2015-3952

1) The magnitude of accuracy variability was greater with heated flow than with unheated flow.
2) Flow rate off scale low readings were a random occurrence with significant frequency under heated conditions which could possibly be associated with bubble formation (see Fig. 31).
3) The UFM flow rate measurement varied with temperature (see Fig. 32).
4) Zero-flow offsets were not consistent, and in many cases, it was difficult to establish stability.

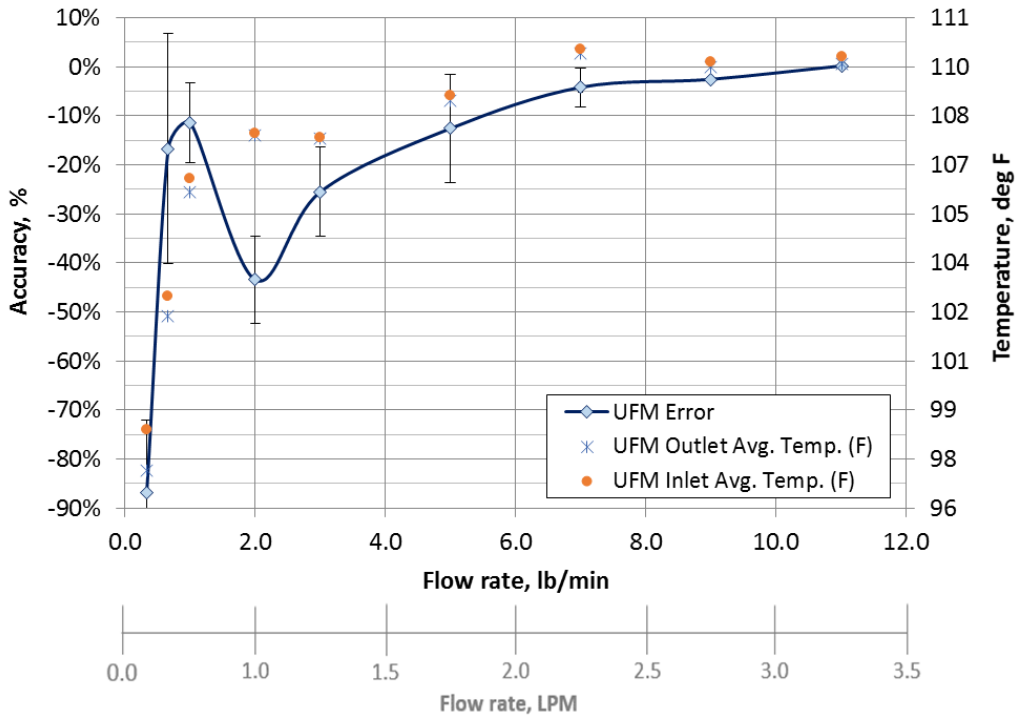

Figure 30. UFM accuracy during heated CFC-113 transfer.

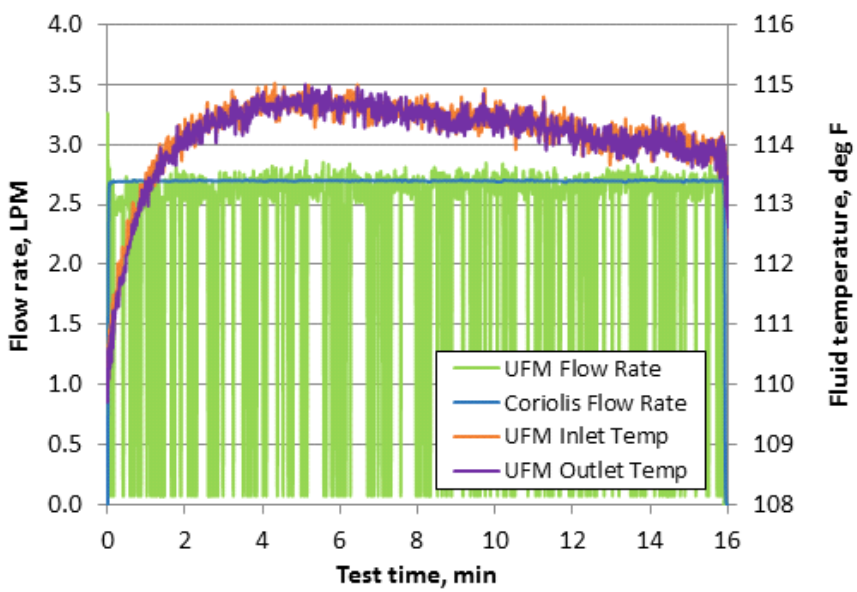

Figure 31. Example of UFM data off scale low readings during heated CFC-113 transfer.

Downloaded by NASA Kennedy Space Center on July 29, 2015 | http://arc.aiaa.org | DOI: 10.2514/6.2015-3952

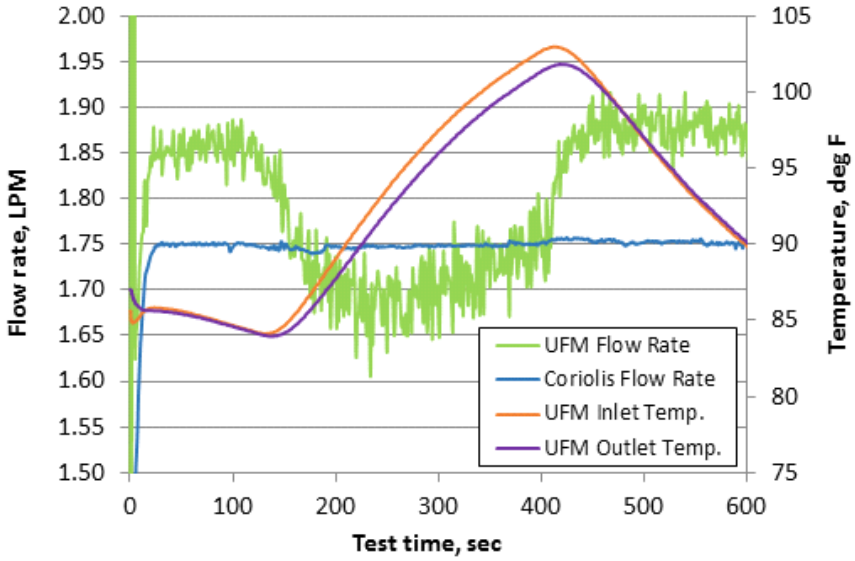

Figure 32. Example of UFM flow rate variation due to temperature variation.

Finally, a limited set of CFC-113 transfers using pumps were performed. The data for these transfers is shown in Fig. 33. The number of transfers per given flow rate was limited to one run, so the data set is of limited value and should be considered only qualitative; however, it can be noted that the accuracy trend as a function of flow rate is very similar to the pressure-fed transfers.

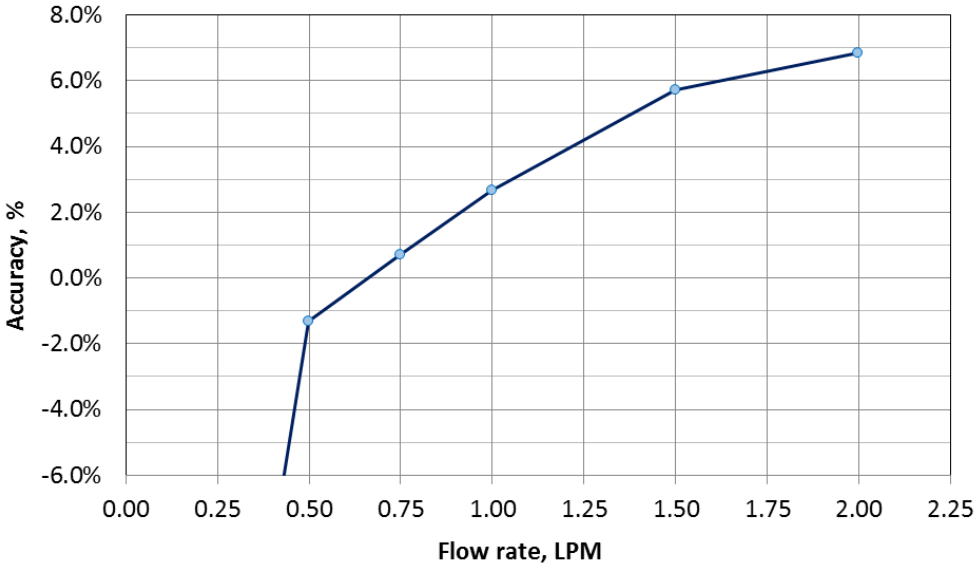

Figure 33. UFM test data, CFC-113 ambient temperature, maximum delta-pressure pump transfer.

b UFM NTO TEST RESULTS

NTO testing used a similar setup to CFC-113 testing, with calibrated primary and secondary standards. The NTO data set was smaller (20 total test runs). The NTO test data was generated in a consistent (and controlled) environment in a relatively short time period (one shift). The data set was limited to 11 lb transfers. Data was obtained for 44 lb transfers, but the ultrasonic meter spontaneously detuned to the point where the meter signal exhibited significant error (totalized mass was only 10% of standard). The motive force for fluid flow was provided by pumps during NTO testing. However, like CFC-113 testing, flow rates were near constant over a given total

Downloaded by NASA Kennedy Space Center on July 29, 2015 | http://arc.aiaa.org | DOI: 10.2514/6.2015-3952

transfer amount. Fig. 34 shows results for UFM NTO testing with pumps (it also shows CFC-113 data for reference). Table 5 tabulates UFM accuracy data for the NTO ambient temperature pump-fed transfers.

The flow rate decrease phenomenon was not observed during the NTO maximum delta-pressure pump-fed testing, and the corresponding low flow rate accuracy was substantially better. The reason for this is not understood at the present time.

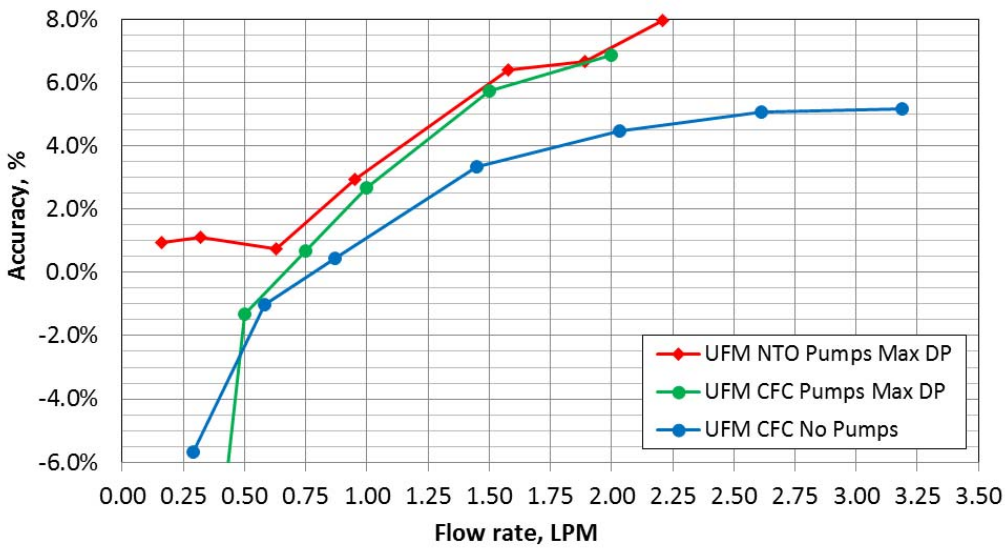

Figure 34. UFM accuracy results for CFC-113 and NTO testing.

Table 5. UFM test data, NTO ambient temperature maximum delta-pressure pump transfers.

Number of Runs (n)	Flow Rate (lb/min)	Average UFM Accuracy	UFM Standard Deviation
3	0.51	0.94%	0.88%
3	1.02	1.12%	0.42%
3	2.01	0.74%	0.12%
3	3.03	2.94%	0.35%
3	5.03	6.40%	0.36%
3	6.02	6.68%	0.16%
2	7.05	7.98%	0.68%

Total=20

3 UFM Performance Summary

Overall, the UFM did not perform as advertised and would not satisfy current project goals. Based on observed test data, the following findings can be made:

Medium-Dependent Volumetric Calibration

The UFM signal-to-flow rate relationship appears to be dependent on the fluid medium. The UFM volumetric flow calibration was advertised as medium independent, but test data for both CFC-113 and NTO show a significant error from manufacturer supplied calibration. Furthermore, the error was flow-rate dependent, non-linear, and can be considered fairly repeatable under controlled conditions at higher flow rates. It was noted that the manufacturer had historically tested the meter accuracy performance using water, ethanol, or hydrazine (all of which have similar fluid properties). CFC-113 entailed a larger flow Reynolds number than water (for the 3/8" flow meter tube) as shown in Table 6 (constant volumetric flow rate; factor of 2 larger) and Table 7 (constant mass flow rate; factor of 1.5 larger).The Reynolds number differences are caused by the differences in density and viscosity of the fluid. In most of the cases the Reynolds number range indicates that the internal flow is turbulent.

Downloaded by NASA Kennedy Space Center on July 29, 2015 | http://arc.aiaa.org | DOI: 10.2514/6.2015-3952

Table 6. Fluid property comparison for water and CFC-113 at constant volumetric flow rate.

Vol. Flow Rate (LPM)	Density @ 20 ºC (kg/m³)		Mass Flow (kg/s)		Reynolds Number		Fluid Velocity (m/s)
	Water	CFC-113	Water	CFC-113	Water	CFC-113	Water or CFC-113
4.0	1003.4	1583.1	0.067	0.106	13515	30522	0.161
3.0			0.050	0.079	10136	22886	0.121
2.0			0.033	0.053	6759	15259	0.081
1.0			0.017	0.026	3380	7629	0.040

Table 7. Fluid property comparison for water and CFC-113 at constant mass flow rate.

Mass Flow Rate (kg/s)	Density @ 20 ºC (kg/m³)		Vol. Flow Rate (LPM)		Reynolds Number		Fluid Velocity (m/s)	
	Water	CFC-113	Water	CFC-113	Water	CFC-113	Water	CFC-113
0.100	1003.4	1583.1	5.98	3.79	20208	28922	0.241	0.153
0.070			4.19	2.65	14144	20243	0.169	0.107
0.040			2.39	1.52	8080	11564	0.097	0.061
0.010			0.60	0.38	2016	2886	0.024	0.015

It is unclear to what extent the Reynolds number difference between water and CFC-113 impacted the validity of the calibration curve; however, according to Temperley et al.[35], the accuracy of an ultrasonic flow meter is affected by flow non-uniformities, flow unsteadiness, turbulence, flow separation, reattachment, recirculation, etc. The normal recommendation for the positioning of ultrasonic sensors is to have sufficiently long, straight upstream and downstream piping to minimize the impact of upstream and downstream hydraulic effects on the region where the ultrasonic sensors are located. The design of the tested meter does not follow this recommendation. To numerically investigate these matters, a CFD model of the UFM was generated with flow rate at a notional value. Regions of flow separation of and recirculation were observed. The CFD analysis proved that the flow field is particularly complex at the flow tube entry junction. Since for a given volumetric flow rate the Reynolds number of CFC-113 (or NTO) differs from that of water, and the Reynolds number in the approach tube differs from that of the flow tube, it is conceivable that varying flow regimes and Reynolds numbers may be affecting the readings, given that the acoustic path is directly down the central axis of the flow tube.

Assuming the flow field is repeatable, it is possible to calibrate the meter with the fluids used for a propellant servicer; however, the cost and risk associated with this approach is considered unacceptable, as the calibration operation itself would be considered hazardous. Nevertheless, the data gathered during this test program suggests the accuracy range may still be outside the bounds of projected goals for certain flow rates.

Sensitivity to Temperature Variations.

Every effort was made to follow the manufacturer's recommendation to keep both transmitting and receiver transducers at a stable and consistent temperature. Most of the testing was carried out at ambient temperature but the heated testing with CFC-113 yielded results that differed significantly from those at ambient temperature, with a substantial number of off-scale low readings. The manufacturer could not characterize the sensitivity of the device to such minor deviations in temperature; therefore, any application of the unit would require empirical correlations that would necessitate extensive testing. Given the sensitivity to temperature, the UFM would not satisfy the projected goals.

Frequent Retuning

Re-tuning was required at least three times during the test program at KSC. It is not known why de-tuning occurred. To mitigate the risk of spontaneous de-tuning during propellant servicing operations, some capability to auto-tune or remote-tune would be required. To our knowledge, this capability does not currently exist, and would likely require a development and verification program that would add unacceptable cost and schedule to a propellant servicer application.

Downloaded by NASA Kennedy Space Center on July 29, 2015 | http://arc.aiaa.org | DOI: 10.2514/6.2015-3952

Downloaded by NASA Kennedy Space Center on July 29, 2015 | http://arc.aiaa.org | DOI: 10.2514/6.2015-3952

Sensitivity to Two-Phase Flow or Saturated Propellants

It was known prior to the test program that the meter would display sensitivity to bubbles, primarily due to signal attenuation and its sensitivity to helium saturated propellants. On account of the test limitations associated with actually re-creating (and verifying) the propellant servicing conditions, it if the meter would be suitable for the intended purpose in this regard.

During the initial meter fill with helium saturated NTO, the meter would not indicate correctly. Extensive tubing bubble sweeping at relatively high liquid flow rates is not a viable solution for on-orbit operations, thus the ultrasonic in-line meter should be considered unsuitable for those applications where dynamic pressures are encountered while the meter is filled with helium saturated propellants.

D. BFM Tests

A balanced orifice flow meter (BFM) was also tested during the PTA test campaign. Initially it was considered to be the second possible candidate flow meter technology for satellite servicing on the basis of its simplicity and advertised performance. A custom-designed multi-hole orifice was fabricated by NASA-MSFC for the test campaign. The meter had a nine-hole orifice as shown in Fig. 35.

It was known prior to testing that this particular BFM was pushing the limits of this technology in that it was possibly not going to be able to achieve the 0.5% accuracy goal at low flow rates. As expected, the pressure drop for the unit was low (on the order of 0 to 5 psid), which would have been acceptable for a flight application; however, test data indicated that the meter would not be able to achieve 0.5% accuracy with repeatable results at flow rates less than approximately 2 lbs/min (1 LPM) as shown in Fig. 42. This is evident from flow physics, e.g. the pressure drop asymptotically approaches zero as the flow rate decreases. As a result, the turndown ratio is poor for this technology (at least for units designed for use at low flow rates).

Figure 35. BFM orifice plate photograph.

E. Coriolis Tests

1 Coriolis Flow Meter Setup: Calibration and Data Processing

The Coriolis flow meter utilized for testing was a commercial off-the-shelf product. There was no modification performed on the meter in any way to meet the propellant servicer design goals. It is understood that there would be modification(s) required to enable the ground-based Coriolis meter that was tested suitable for a space-flight application. It is assumed that these modification(s) are possible and would not significantly impact the performance of the meter.

At the test sites, the unit under test (reference designator FM-03) had a nominal internal tube size of ¼". Prior to use, the meter was calibrated at a NIST-traceable off-site facility. Both the mass flow rate and volumetric flow rate channels were characterized. The mass flow rate channel current output (4-20 mA) was related to the standard's mass flow rate by a linear equation. The calibration did not include a zero-flow condition, but the derived line slope is within 0.02% of the theoretical span and the equation was within 0.03% (as % of reading) of all calibration points. The data channels selected for recording were mass flow rate and fluid density. At the second NTO test, one channel was employed for temperature. Also at the second NTO test, two additional meters were added to the test setup, FM-06 and FM-07. FM-07 was functionally similar to FM-03 and FM-06 was a smaller unit (nominal line size 1/6"). For comparison, FM-06 maximum flowrate was 15% of FM-03's maximum flowrate, but nominal flowrate (the flow rate required to create a pressure drop of 14.5 psid with water) was 23% of FM-03. FM-06 was selected to determine if decreasing nominal line size would offer improved accuracy for some of the test runs at lower flow rate.

Both FM-06 and FM-07 were calibrated at the manufacturer. The FM-06 output was linear with flow rate over the entire flow range. FM-07 was rescaled to provide output over a sub-set (0 to 15 lbs/min) of the full calibrated range (0 to 40 lbs/min). A calibration of these two meters following the second NTO test revealed that this method was reasonable.

Downloaded by NASA Kennedy Space Center on July 29, 2015 | http://arc.aiaa.org | DOI: 10.2514/6.2015-3952

2 Coriolis Test Results

The Coriolis meter FM-03 performed similarly in both CFC-113 and NTO, under varying flow conditions and transfer amounts. Fig. 36 shows FM-03 meter performance in the CFC-113 non-pump (needle flow control valve) transfers. The error bars show total span of data points for a given flowrate and transfer amount. After dozens of test runs at various flow rates, transfer quantities, inlet/outlet pressures, temperatures, with CFC-113 and NTO, it can be stated that 0.5% accuracy can be achieved with a Coriolis flow meter above about 1 lb/min. It is not clear at the present time as to why the accuracy degrades below a flow rate of about 1 lb/min, especially considering most Coriolis flow meter manufacturers advertise a 1:100 turndown ratio. Fig. 37 shows flow meter accuracy for CFC-113 pump transfers. Parameters within the two different pumping modes (constant flow rate and constant RPM) were found to have minimal impact on the Coriolis flow meter accuracy as noted on Fig. 37. FM-06 and FM-07 also yielded comparable performance as shown in Fig. 38.

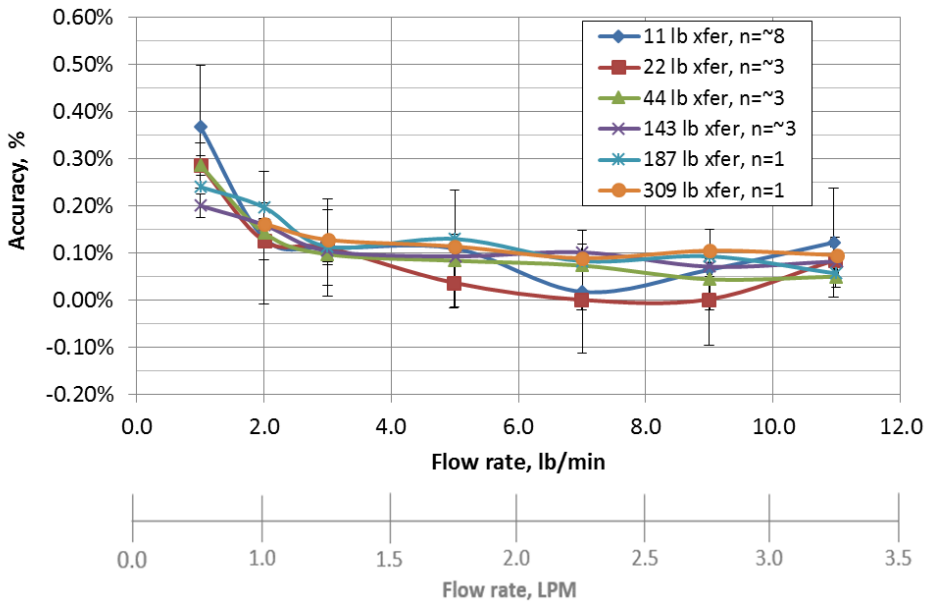

Figure 36. Coriolis (FM-03) CFC-113 test results, needle flow control valve runs (139 total runs).

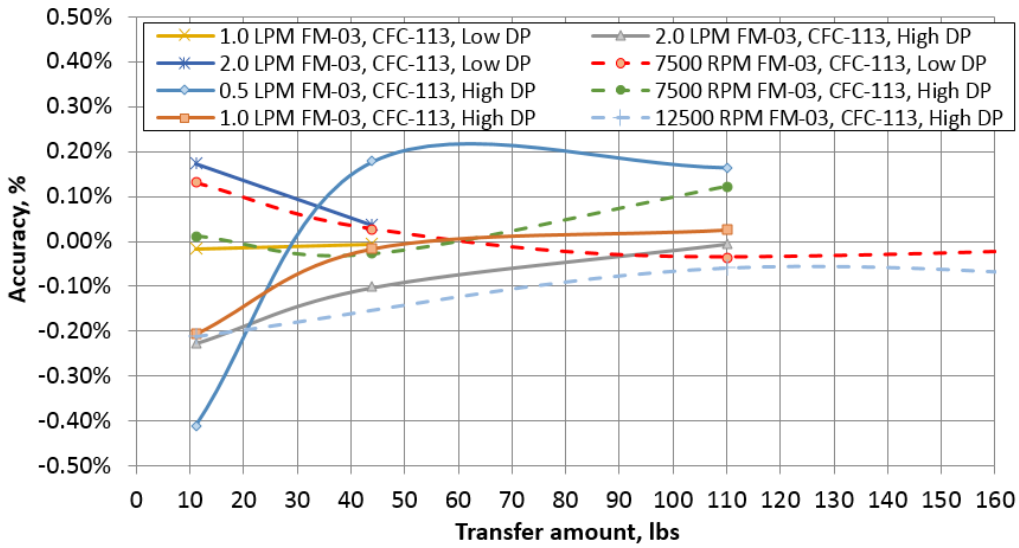

Figure 37. Coriolis (FM-03) accuracy as a function of pump transfer method and transfer amount.

Downloaded by NASA Kennedy Space Center on July 29, 2015 | http://arc.aiaa.org | DOI: 10.2514/6.2015-3952

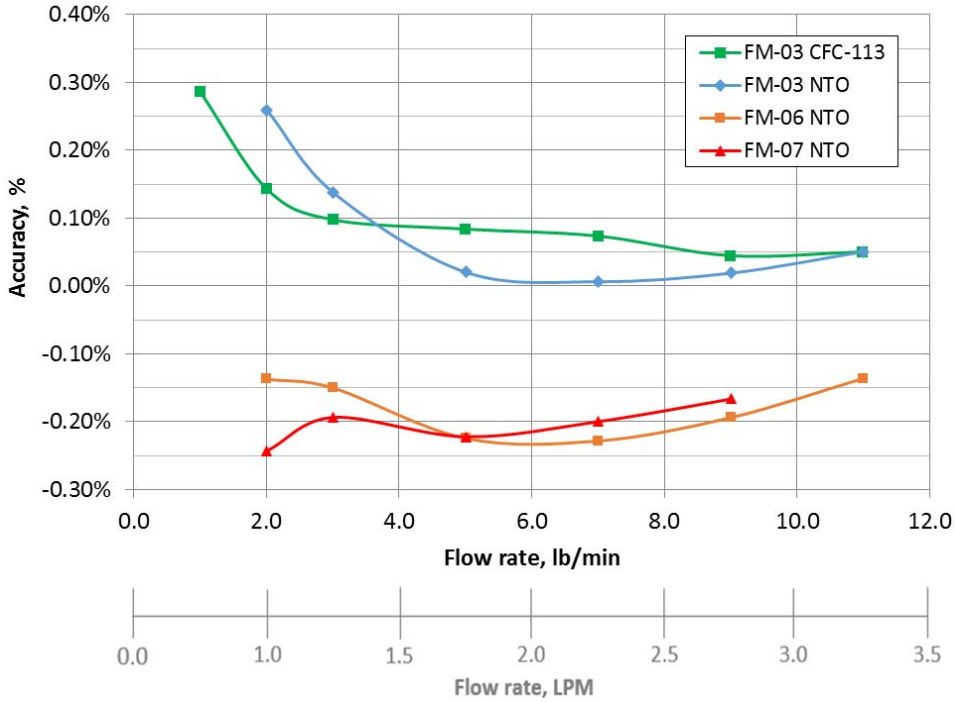

Figure 38. Coriolis flow meter accuracy for 44 lb transfer (NTO and CFC-113).

The offsets due to maximum delta-pressure conditions (shown Fig. 37 and Fig. 39) are believed to be due to fluid dynamic effects, and not an aspect of meter performance per se. The Coriolis flow meter achieved the best accuracy, but exhibited an offset when the system was tested with a high pressure differential generated by the pumps. The offset is an artifact of the following factors: the Coriolis flow meter output was not scaled to record reverse flow in the data file; the totalizer software does not totalize signals below the pre-set "noise" threshold; therefore, negative flow readings were not be "subtracted" from the totalized mass, and transient effects associated with flow termination under high delta pressure.

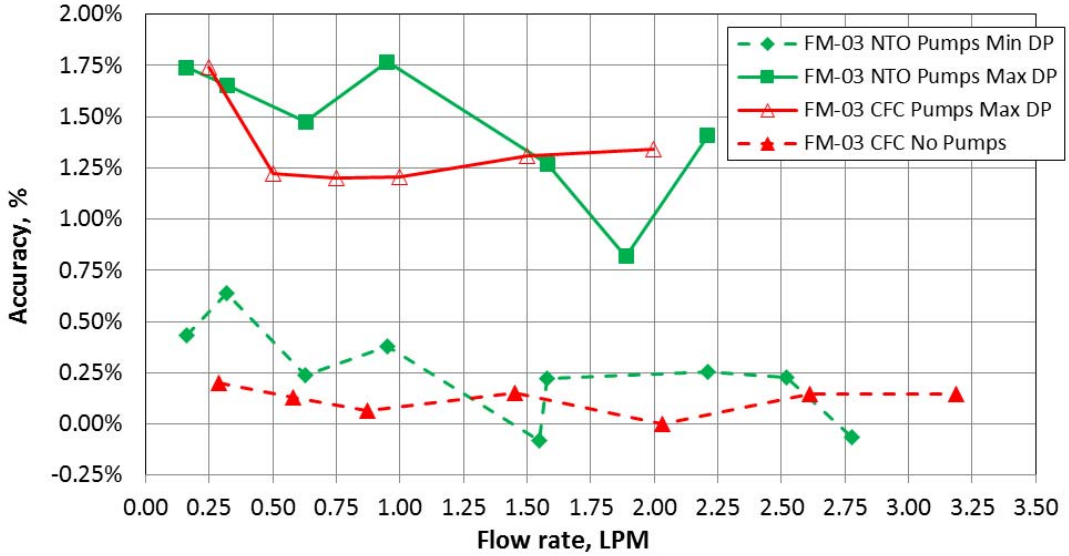

Figure 39. Coriolis flow meter anomaly during high delta-pressure pump runs.

During the early stages of testing that the Coriolis flow meters exhibited significant latency in response to flow changes specifically at the beginning and ending of flow (as noted in Fig. 40 and Fig. 41). The totalizer implementation allows for totalization even after the shut-off valve is closed, allowing this transient to be accounted for; however, as mentioned previosly, if the flow was reveresed upon valve closure, the negative flow was not accounted for in the totalization.

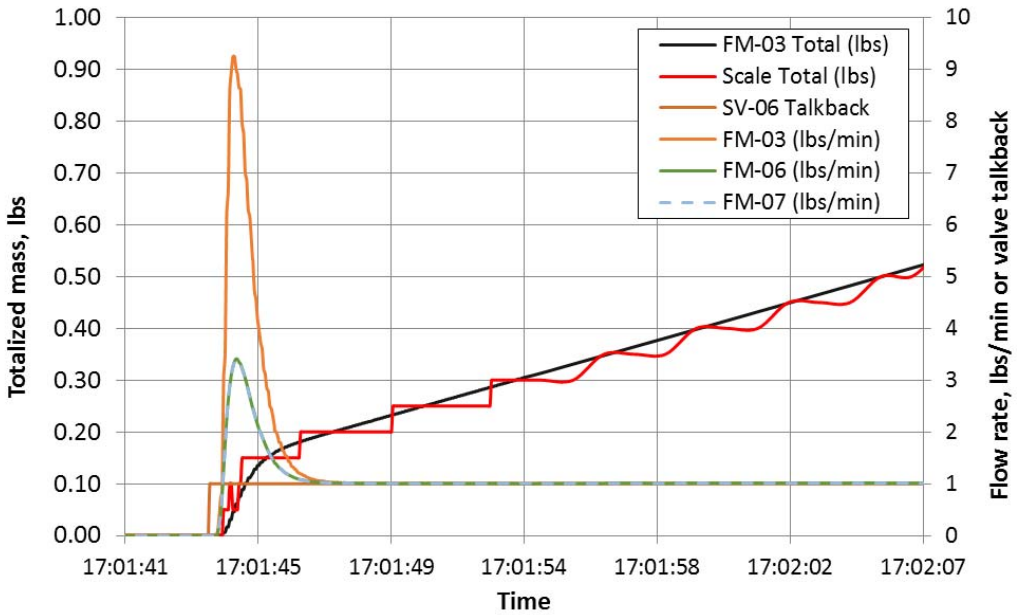

Figure 40. Coriolis flow meter flow start latency example.

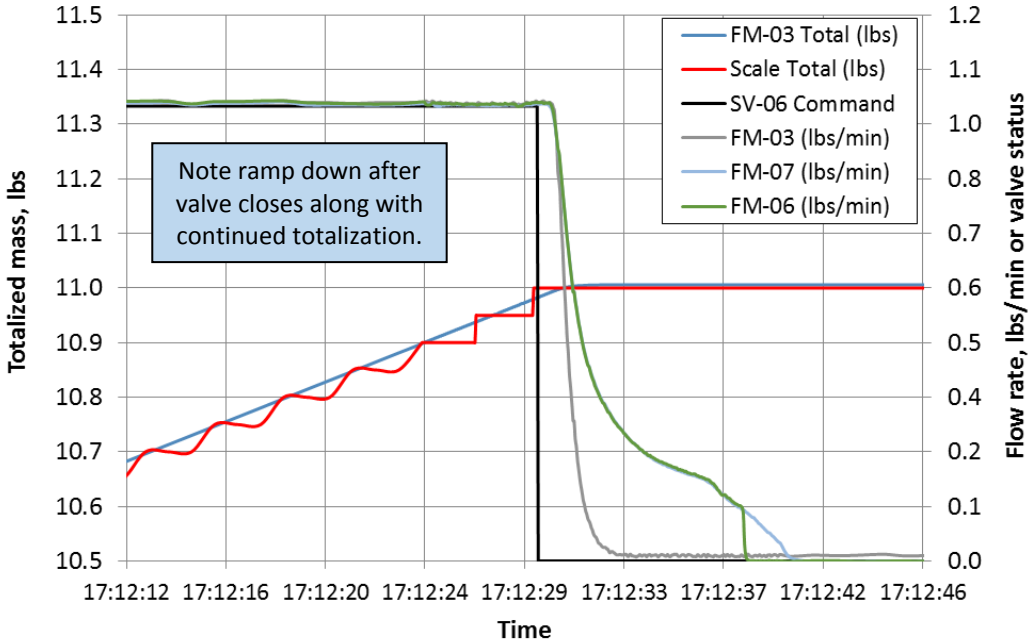

Figure 41. Coriolis flow meter flow termination latency example.

Downloaded by NASA Kennedy Space Center on July 29, 2015 | http://arc.aiaa.org | DOI: 10.2514/6.2015-3952

Downloaded by NASA Kennedy Space Center on July 29, 2015 | http://arc.aiaa.org | DOI: 10.2514/6.2015-3952

3 Coriolis Performance Summary

The Coriolis flow meters performed quite well during the test campaign. As expected, the Coriolis units were found to be medium-independent, insensitive to temperature variations, and not highly sensitive to flows with saturated propellants. However, the latency of the Coriolis flow meter may impact the totalized mass accuracy, depending on how the totalizer is designed.

It was found that each Coriolis flow meter had a different start/stop transient fingerprint. For smaller mass transfers (below about 20 lbs), and higher supply to return pressure differentials (exceeding about 75 psid), the impacts of start/stop transients and system parameters are of greater relative significance. For larger transfers (greater than about 50 lbs), these items are "in the noise" of the accuracy calculation.

Furthermore, most Coriolis flow meters afford a second data output that could include the totalized mass, fluid temperature, fluid density in addition to mass flow rate. Specifically, the temperature and fluid density data streams would be useful in most setups possibly eliminating additional instrumentation.

The Coriolis flow meter does have risks since it has never been proven in a space flight (and launch) environment. Baird[30] found that the Coriolis flow meters accuracy worsened when tested in a micro gravity environment compared to ground testing. It is unclear from the report as to why this was the case, however this situation could have been a result of start/stop transient affects since the parabolic aircraft flight test sequences were only about 20 seconds long (at most). Additionally, qualification of the electronics and other active hardware would need to be performed prior to flight along with a necessary mass reduction effort to convert a ground based unit to a flight version.

F. Comparison of Flow Meter Performance

Fig. 42 summarizes the testing results from 29 separate runs for the nominal 11 lb transfer runs at ambient fluid temperature. On the basis of these results, it is possible to characterize the relative performance of the flow meters under consideration.

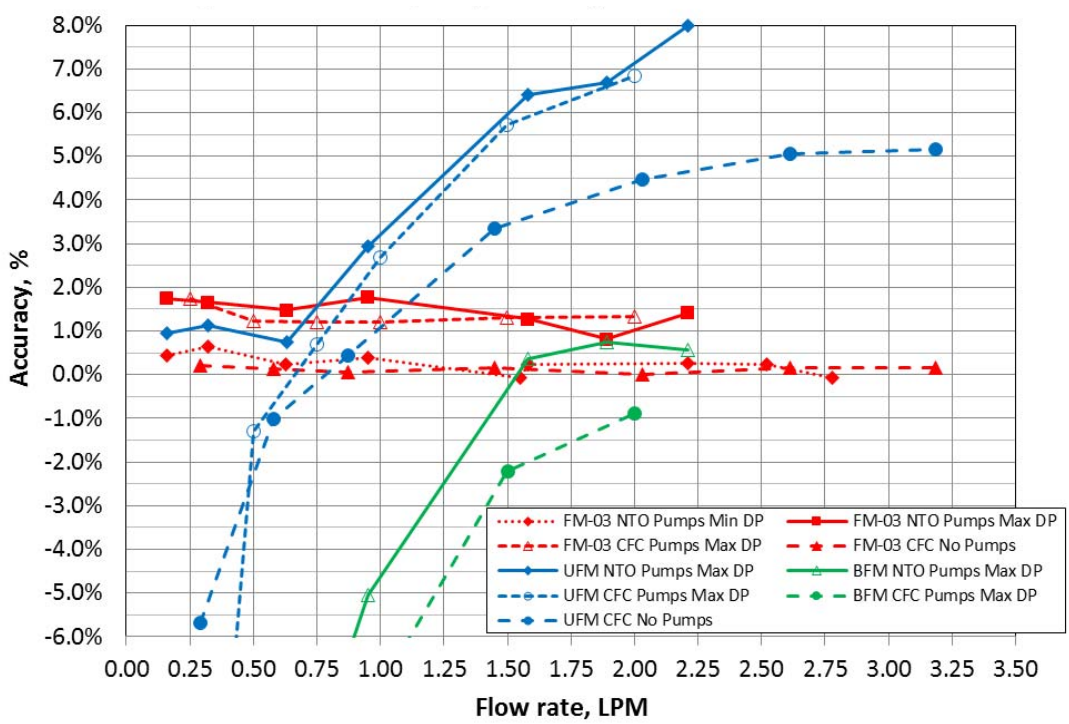

Figure 42. Performance comparison of and UFM, BFM, Coriolis, with CFC-113 and NTO at ambient temperature.

The accuracy of the UFM was found to be strongly dependent on flow rate and exhibited poor repeatability at flow rates less than 3 lbs/min (as shown in Fig. 28); therefore, it is deemed unacceptable for the application under consideration. In the BFM case, the accuracy was sensitive to flow rate and commodity type, thus the flow meter

does not fulfill the design goals. The Coriolis flow meter afforded the highest accuracy, but exhibited an offset at a high pressure differential generated by the pumps. As previously mentioned, this offset arose from factors such as lack of totalization below the pre-set "noise" threshold, and transient effects (associated with flow termination).

Table 8 provides a summary of the performance of the various flow meters. Generally the UFM accuracy was highly dependent on flow rate. Thus the in-line ultrasonic flow meter that was tested was deemed unacceptable for the PTS application. The observed BFM accuracy was sensitive to flow rate and commodity type, and was also determined unsuitable for the application. The Coriolis flow meter achieved the best accuracy of the three flow meters and was found to be the best candidate to meet the application goals pending further study on space-flight qualification and the impacts of micro gravity on the unit's accuracy.

Table 8. Summary of test results.

	UFM	BFM	Coriolis
Accuracy of 0.5% or better	Failed	Failed	Passed
Same design compatible and operable with N_2O_4, MMH, and N_2H_4	Failed*	Passed*	Passed*
Able to measure volumetric flow rates from about 0 to 6 LPM	Passed	Passed	Passed
Able to operate at commodity temperatures of 10-50 deg. Celsius	Failed	Passed	Passed
Able to withstand geosynchronous earth or low earth orbit operational environment	Unknown (but partially qualified)	Unknown	Unknown (future work)
Able to withstand external load environments during launch and flight	Unknown (but partially qualified)	Unknown	Unknown (future work)

*Only tested with N2O4; verification of performance with MMH and N2H4 is future work

G. Summary of Flow Meter Testing

A detailed test campaign studying the implications of various parameters consistent with the PTS took place. It is known that much work remains ahead to create a flight-qualified highly accurate flow meter; however, many initial flow meter technology features have now been realized and proven via testing with a simulant fluid and nitrogen tetroxide.

IV. Future Work

A. Vent Dispersion

As an extension of the present efforts, a lethal service (hypergol) vacuum chamber is being acquired to carry out laboratory experiments with water (serving as calibration for our test setup and instrumentation) and hypergols and other possible fluids of interest for satellite servicing. The theoretical models in conjunction with the new test data would enable optimization of the nozzle and orifice configurations and jet parameters pertinent to the propellant transfer system.

B. Flow Meter Testing

An expanded test campaign is already in the late planning/early execution phases. The lessons that were learned in the first phase of testing are being applied directly to the second evolution of the test setup. An alternate UFM design being considered for testing along with alternate Coriolis flow meter manufacturers. There are also plans of testing a Coriolis flow meter on the International Space Station on a potential future mission.

Downloaded by NASA Kennedy Space Center on July 29, 2015 | http://arc.aiaa.org | DOI: 10.2514/6.2015-3952

Downloaded by NASA Kennedy Space Center on July 29, 2015 | http://arc.aiaa.org | DOI: 10.2514/6.2015-3952

V. Conclusions

A. Vent Dispersion Modeling

The proposed model for bubble growth in flashing liquid jets is shown to describe satisfactorily the test data characterizing the jet burst distance and the burst cone angle for dispersion. It is shown that the jet burst distance increases with a decrease in jet initial temperature, and decreases with a decrease in jet initial velocity. The postulated criterion that the jet bursts when the bubble radius grows to a size four times that of the jet radius has been demonstrated.

B. Propellant Mass Flow Measurement Testing

The lengthy flow meter test campaign provided valuable data to the PTA design team. The major characteristics of different flow meter technologies have been identified and can be directly applied to the design of a flight system through a rigorous qualification test program. It is believed that the Coriolis flow meter technology will best suit the needs of the storable propellant PTA system design and potentially other propellants, but other candidates are still under consideration that have not been tested to date.

VI. Appendix A

The study documented by Baird[30] was scrutinized to determine if relevant data could be utilized for the application of an on-orbit propellant transfer system. This report covered various flow metering concepts and characterized capabilities and limitations of flow meters for on-orbit fluid transfer operations. The basic operating principles of each of the flow meters evaluated were summarized, and selection criteria for the best flow meter(s) for each application were reported. The tested flow meter technologies included, clamp-on ultrasonic, area averaging ultrasonic, offset ultrasonic, Coriolis mass, vortex shedding, universal venturi tube, turbine, bearing-less turbine, turbine/turbine differential pressure hybrid, drag-body, and drag-body/turbine hybrid flow meters. Many flow meter selection considerations were reported and are discussed including performance, fluid operating conditions, system operating environments, packaging, maintenance, and overall technology.

The Baird testing campaign was performed on the ground and also using a portable flow test stand that was installed on a zero-g (micro gravity) capable aircraft (KC-135). The portion of testing on the KC-135 was repeatedly maintained down to accelerations of 0.02 g for periods of 17 to 20 seconds as shown in Fig. 43.

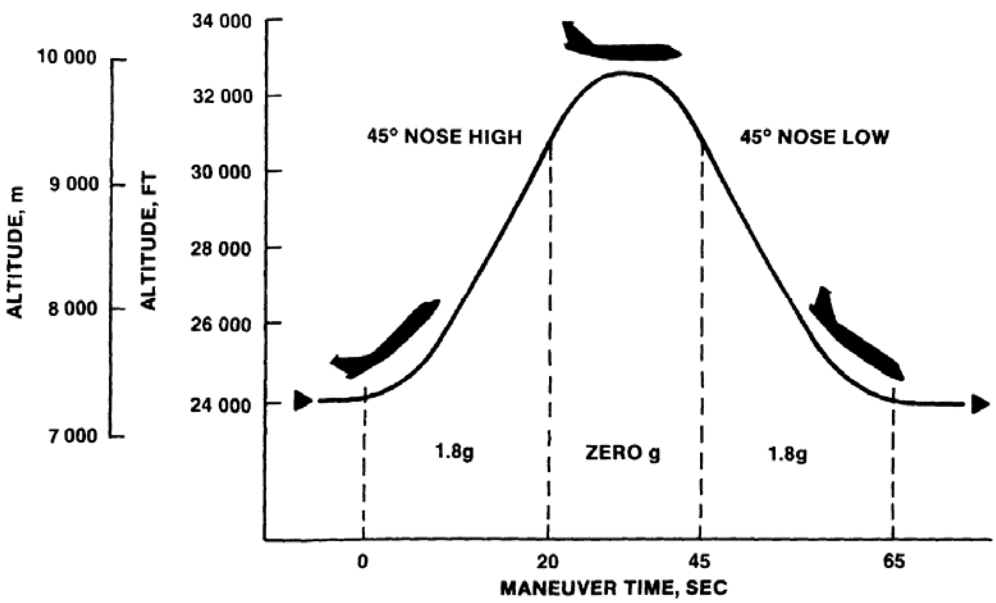

Figure 43. KC-135 aircraft trajectory and zero-g environment.

As shown in the data from Baird[30], the units were thoroughly tested at various parameters, some of which were similar to the testing that was reported in this paper and others which will need further study in the future (vibration

impacts, pulse flow impacts, and gas ingestion). It has been previously noted that based on evaluation criteria and the various considerations when selecting a flow meter for on-orbit operations that no single flow meter concept has been shown to best fit all applications for on-orbit fluid transfer operations and that a detailed selection process must be performed. There are generalizations that may be made from the extensive testing completed on the ground by Baird[30] during KC-135 flight testing. Rigorous testing and detailed analytical models may be setup in the future to help the down-select process for the types of flow meters that meet the specific on-orbit environments identified in the propellant transfer system goals.

VII. Acknowledgments

This work was funded by NASA Goddard Space Flight Center in partnership with NASA Kennedy Space Center. The experimental support of Kevin Abbott of Jacobs Engineering, Wes Mosedale, Slade Peters, Phil Stroda, Erik Tormoen, and Cara Evers of NASA Kennedy Space Center with regard to flow meter testing is gratefully acknowledged. Gabriela Escalera of Kennedy Space Center (NE-F) generated the CFD results for the UFM. The authors also thank Melissa Mierzwa of Sierra Lobo Inc. for her assistance in the preparation of the manuscript.

VIII. References

[1]Fuchs, H., and Legge, H., "Flow of a water jet into vacuum," *Acta Astronautica*, Vol. 6, 1979, pp.1213-1226.

[2]Blander, M., and Katz, J.L., "Bubble nucleation in liquid," *AIChE Journal* , Vol. 21, No. 5, 1975, pp. 833-848.

[3]Sher, E., Bar-Kohany, T., and Rashkovan, A., "Flash boiling atomization," *Prog. Energy Combustion*, Vol. 34, 2008, pp.417-439.

[4]Muntz, E.P., and Orme, M., "Characteristics, control, and use of liquid streams in space," *AIAA Journal*, Vol. 25, No. 5, 1987, pp. 746-756.

[5]Collier, J.G., *Convective Boiling and Condensation*, 2nd ed., McGraw-Hill, New York, 1981.

[6]Lee, H.S., Merte, Jr., H., "Spherical vapor bubble growth in uniformly superheated liquids," *International Journal of Heat and Mass Transfer*, Vol. 39, No. 12, 1996, pp. 2427-2447.

[7]Lord Rayleigh, "On the pressure developed in a liquid during the collapse of a spherical cavity," Philosophical Magazine, Vol. 34, 1917, pp. 94-98; Scientic Papers, Cambridge University Press, Vol. 6, 1920, p. 504.

[8]Plesset, M.S., "The dynamics of cavitation bubbles," *ASME Journal of Applied Mechanics*, Vol. 16, 1949, pp. 228-231.

[9]Forster, H.K., and Zuber, N., "Growth of a vapor bubble in a superheated liquid," *Journal of Applied Physics*, Vol. 25, No. 4, 1954, pp. 474-478.

[10]Plesset, M.S., and Zwick, S.A., "A nonsteady heat diffusion problem with spherical symmetry," *Journal of Applied Physics*, Vol. 23, 1952, p.95.

[11]Plesset, M.S., and Zwick, S.A., "The growth of vapor bubbles in superheated liquids," *Journal of Applied Physics*, Vol. 25, No. 4, 1954, pp. 493-500.

[12]Birkhoff, G., Margules, R.S., and Horning, W.A., "Spherical bubble growth," *Physics of Fluids*, Vol. 1, 1958, p. 201.

[13]Scriven, L.E., "On the dynamics of phase growth," *Chemical Engineering Science*, Vol. 10, 1959, pp. 1-13.

[14]Mikic, B.B., Rohsenow, W.M., and Griffith, P., "On bubble growth rates," *International Journal of Heat and Mass Transfer*, Vol. 13, 1970, pp. 657-666.

[15]Miyatake, O., Tanaka, I., and Lior, N., "A simple universal equation for bubble growth in pure liquids and binary solutions with a nonvolatile solute," *International Journal of Heat and Mass Transfer*, Vol. 40, No. 7, 1997, pp. 1577-1584.

[16]Prosperetti, A., Plesset, M.S., "Vapor-bubble growth in a superheated liquid," *Journal of Fluid Mechanics*, Vol. 85, 1978, pp. 349-368.

[17]Theofanous, T.G., and Patel, P.D., "Universal relations for bubble growth," *International Journal of Heat and Mass transfer*, Vol. 19, 1976, pp. 425-429.

[18]Schulz, D.L., and Jones, T.V., "Heat transfer measurements in short duration hypersonic facilities," AGARDOgraph 165, 1973.

[19]Aldred, J.W., Smith, L.N., Wang, K.C., Lumpkin, F.E., and Fitzgerald, S.M., Modeling of water injection into vacuum, AIAA-98-2588 (1998).

[20]Wildgen, A., and Straub, J., "The boiling mechanism in superheated free jets," *International Journal of Multiphase Flow*, Vol. 15, No. 2, 1989, pp. 193-207.

[21]Lien,Y.C., Bubble growth rates at reduced pressure, D.Sci. Thesis, MIT (1969).

[22]Dergarabedian, P., "The rate of growth of vapor bubbles in superheated water," *Journal of Applied Mechanics*, Vol. 20, 1953, pp. 537-545.

[23]Mann, B.L., and Stoll, O.T., "Experimental investigation of the freezing problem present in discharging water present in discharging water based fluids to space," Society of Automotive Engineers, 912 D (1964).

[24]Kitamura, Y., Morimitsu, H., and Takahashi, T., "Critical superheat for flashing of superheated liquid jets," *Industrial Engineering Chemistry Fundamentals*, Vol. 25, 1986, pp. 206-211.

Downloaded by NASA Kennedy Space Center on July 29, 2015 | http://arc.aiaa.org | DOI: 10.2514/6.2015-3952

[25]Steddum, R., Maples, D., and Donovan, F.M., "Investigation of the characteristics of fluids vented into vacuum," *NBS Space Simulation*, Vol. 56, 1970, pp. 905-914.

[26]Mikatarian, R.R., and Anderson, R.G., "An experimental investigation of a liquid jet expelled into vacuum," *Journal of Spacecraft and Rockets*, Vol. 3, No. 20, 1966, pp. 267-268.

[27]Griffith, P., "Bubble growth rates in boiling," *Transactions of the ASME*, Vol. 80, 1958, p.721.

[28]Cole, R., and Shulman, H.L., "Bubble growth rates at high Jacob numbers," *International Journal of Heat and Mass Transfer*, Vol. 9, 1966, pp. 1377-1390.

[29]Kandula, M., Mechanisms and predictions of burnout in flow boiling over heated surfaces with an impinging jet, *International Journal of Heat and Mass Transfer*, Vol. 33, No. 9, 1990, pp. 1795-1803.

[30]Baird, R. S.: *Flowmeter Evaluation for On-Orbit Operations*. NASA Lyndon B. Johnson Space Center Technical Memorandum 100465, Aug. 1988.

[31]Werlink, Rudolph, Harry Johnson, and Ravi Margasahayam. *Nonintrusive Flow Rate Determination Through Space Shuttle Water Coolant Loop Floodlight Coldplate*. NASA TM-112443. January 1997.

[32]Werlink, Rudolph, Andrew Kelly, and Ravi Margasahayam. *Space Shuttle Hypergol Load Determination Using Nonintrusive Ultrasonic Flow Meters*. NASA TM-111884. October 1996.

[33]Lotters, Joost C et. al. *Micro Coriolis Mass Flow Sensor with Extended Range for a Monopropellant Micro Propulsion System.* AMA Conferences 2013 – Sensor 2013, OPTO 2013, IRS 2013. DOI 10.5162/sensor2013/D2.4. 2013.

[34]Kelley, Anthony. *Balanced Flow Meter and Conditioning Technology for Fluid Systems (Space Liquid Propulsion Systems).* 2006 Instrumentation Symposium for the Process Industries. http://www.aplusflowtek.com/. November 11, 2005.

[35]Temperley, Neil C, Masud Behnia, and Anthony F Collings. *"Flow Patterns in an Ultrasonic Liquid Flow Meter."* Flow Measurement and Instrumentation, Volume 11, Issue 1. March 2000. pp 11–18.

Downloaded by NASA Kennedy Space Center on July 29, 2015 | http://arc.aiaa.org | DOI: 10.2514/6.2015-3952